Low-Frequency Intensity Modulation of High-Frequency Rotor Noise

Baars, W.J.; Ragni, D.

DOI
10.2514/1.J063610

Publication date
2024

Document Version
Final published version

Published in
AIAA Journal: devoted to aerospace research and development

AIAA JOURNAL
Vol. 62, No. 9, September 2024

Low-Frequency Intensity Modulation of High-Frequency Rotor Noise

Woutijn J. Baars* and Daniele Ragni†
Delft University of Technology, 2629 HS Delft, The Netherlands

https://doi.org/10.2514/1.J063610

Acoustic spectra of rotor noise yield frequency distributions of energy within pressure time series. However, they are unable to reveal phase relations between different frequency components while these play a role in the fundamental understanding of low-frequency intensity modulation of higher-frequency rotor noise. A methodology to quantify interfrequency modulation is applied to a comprehensive acoustic dataset of a fixed-pitch benchmark rotor, operating at a low Reynolds number and at advance ratios ranging from $J = 0$ to 0.61. Our findings strengthen earlier observations in case of a hovering rotor, in which the modulation of the high-frequency noise is strongest around an elevation angle of $\theta = -20°$ (below the rotor plane). For the nonzero advance ratios, modulation becomes dominant in the sector $-45° \lesssim \theta \lesssim 0°$ and is most pronounced at the highest advance ratio tested ($J = 0.61$). Intensity modulation of high-frequency noise is primarily the consequence of a far-field observer experiencing a cyclic sweep through the noise directivity pattern of relatively directive trailing-edge noise. This noise component becomes more intense with increasing J and is associated with broadband features of the partially separated flow over the rotor blades.

Nomenclature

A	=	rotor disk area, πR^2, m^2
a_∞	=	acoustic velocity, m/s
C_T	=	rotor thrust coefficient, $F_z/(\rho A \Omega^2 R^2)$
C_τ	=	rotor torque coefficient, $\tau_z/(\rho A \Omega^2 R^3)$
c	=	blade chord, m
D_p	=	diameter of rotor blades, m
F_z	=	rotor thrust, N
FM	=	figure of merit
f	=	frequency, Hz
f_b	=	blade passing frequency, Hz
f_s	=	sampling frequency, Hz
J	=	advance ratio, $U_\infty/(2\omega R)$
M_{tip}	=	rotor tip Mach number, U_{tip}/a_∞
N	=	data partition size
P	=	rotor power, $2\pi\omega\tau_z$, W
p	=	pressure, Pa
p_∞	=	ambient pressure, Pa
Re	=	Reynolds number
R	=	radius of rotor blades, m
r	=	radial coordinate, m
T_∞	=	ambient temperature, K
t	=	temporal coordinate, s
U	=	mean velocity, m/s
U_{tip}	=	rotor tip speed, m/s
U_∞	=	freestream velocity, m/s
z	=	axial coordinate, m
θ	=	directivity angle, deg
λ	=	acoustic wavelength, m
ρ	=	radial distance in spherical coordinates
ρ_∞	=	air density, kg/m^3
τ	=	temporal coordinate over one rotor revolution, s
τ_z	=	rotor torque, N · m
ϕ	=	angular position of rotor, rad or deg
ϕ_{pp}	=	one-sided acoustic pressure spectrum, Pa^2/Hz
ω	=	rotational speed of the rotor, rev/s or Hz
ω_ϕ	=	in-plane vorticity, 1/s
Ω	=	rotational speed of the rotor, $2\pi\omega$, rad/s

Subscripts

p	=	propeller
r, z, ϕ	=	cylindrical coordinates
ref	=	reference quantify for dB level
∞	=	ambient condition

Superscript

$*$	=	complex conjugate

Presented as Paper 2023-3215 at the AIAA Aviation 2023 Forum, San Diego, CA, June 12–16, 2023. Submitted to the AIAA Journal; received 29 September 2023; revision received 27 March 2024; accepted for publication 28 March 2024; published online 13 May 2024.

*Assistant Professor, Faculty of Aerospace Engineering, Flow Physics and Technology Department, Kluyverweg 1; w.j.baars@tudelft.nl, www.baars-delft.tech. Senior Member AIAA.

†Associate Professor, Faculty of Aerospace Engineering, Flow Physics and Technology Department, Kluyverweg 1; d.ragni@tudelft.nl. Member AIAA.

I. Introduction

URBAN air mobility (UAM) vehicles and drones comprise rotors that are typically smaller than the single-rotor technology of conventional helicopters. For instance, many electrical takeoff and landing (eVTOL) prototype vehicles contain a multitude of rotors, e.g., the Joby Aviation vehicle includes 6 rotors, the EHang 216 autonomous aerial vehicle has 6 rotors, the Supernal SA-1 eVTOL aircraft has 4 tiltrotors and 4 sets of stacked corotating rotors, and the VoloDrone and VoloCity vehicles of Volocopter include 18 rotors each. Assessing the rotor noise of new advanced air mobility (AAM) vehicles has gained a high priority due to their intended operation in densely populated areas [1]. At the same time, engineering studies on the noise impact of rotors should be revisited because time-varying aspects of acoustic waveforms are rarely addressed, while these influence the human perception of rotor noise.

Most studies on the acoustics of small-scale rotors consider standard characterization schemes that rely on time averaging and/or ensemble averaging [2–12]: results are typically condensed to a set of acoustic spectra, their integrated energy (overall sound pressure level, SPL), as well as the directivity patterns of that acoustic energy. These methods are unsuited to assess the *wop-wop* noise component from larger-size rotorcraft or even the higher-frequency *buzzing* noise of drone propellers, since these are often time-varying phenomena of high-frequency noise and not necessarily a direct perception of the blade passing frequency (BPF), denoted as f_b. Current noise certification standards fall short in capturing time-varying aspects (e.g., the tone-corrected, effective perceived noise level (EPNL) and/or the A-weighted sound exposure level (SEL) in 14 CFR Part 36 are

time-averaged metrics). Paradoxically, there is a growing body of knowledge that time-varying noise aspects are highly relevant for the level of psycho-acoustic annoyance [10,13–18]. As such, noise levels that comply with a certification standard are not acceptable to the public per say, and further assessments of noise-perception aspects are needed. In particular, the low-frequency modulation of higher-frequency rotor noise is important for the development of low-order modeling and auralization algorithms [19–21], as well as psycho-acoustic modeling [22–24].

A. Rotor Noise Modulation

Before considering the temporal variation of rotor noise, a short review of noise sources is provided. Periodic rotor noise components are classified as thickness noise and blade loading noise [25–28]. A superimposed component of broadband noise originates from the blade encountering turbulent fluctuations (a leading-edge mechanism) and vortical turbulent boundary-layer motions convecting past the rotor's trailing edge. In addition, for low-Reynolds-number propellers, an additional near-wake source comes from the vortex shedding behind laminar and/or turbulent separation regions [29,30]. And finally, even when the rotor operates in a clean flow, turbulence ingestion noise can become dominant through the onset of blade–wake interaction (BWI). This interaction is determined by the distance between the blade wake and tip vortex deployed by consecutive blades and the blades themselves.

Temporal variations in the acoustic intensity and characteristic frequency of the noise are dubbed intensity (or amplitude) and frequency modulations, respectively. In this work, we consider the intensity modulation and refer to this as BPF modulation (BPFM); it will become evident that its time scale is set by the blade's period of rotation. Hence, the modulation phenomenon at this time scale is fundamentally different from the variations in noise amplitude and Doppler frequency shift that occur in transient rotorcraft flyover maneuvers. In those cases, studies do occasionally employ time-preserving schemes when dealing with nonstationary acoustic signals [31,32]; they focus on *very* long-timescale variations in noise, relative to the BPF time scale, associated with maneuvers of the flight vehicle.

Gan et al. [18] studied temporal variations of rotor noise within the reference frame of a Bell 206 helicopter in level and descending flight, including acoustic and short-time-varying aspects associated with aerodynamic interactions and the noise of the tail rotor. Here, we study the effect of BPFM using an isolated rotor to focus on its source mechanisms. To illustrate BPFM, consider the acoustic spectrum of rotor noise shown in Fig. 1a. The acoustic pressure time series associated with the BPF can be generated using a narrow band-pass filter and is shown in Fig. 1b. When the high-frequency content of the signal is *unmodulated*, the time series after high-pass filtering (in this example $f > 10f_b$) has a time-invariant envelope of the intensity (Fig. 1c). However, due to the rotating nature of the blade's noise sources, a *modulated* intensity envelope may arise. This modulated high-frequency noise is illustrated in Fig. 1d after artificially modulating the carrier signal.

Fundamental source mechanisms of BPFM may initially be thought of as harmonic variations in the source–receiver distance and/or convective amplification (as a direct result of the rotor spinning). Convective amplification of the sound pressure amplitude ($p_{\mathrm{rms}} \propto 1/[1 - M_r \cos\theta]$) is strongly dependent on M_r, the relative Mach number of the source toward the observer and angle θ between the source velocity and the source-observer ray path (e.g., [33]). An increase in sound amplitude when the rotor is nearer the observer and when the observer is forward of the advancing side is thus expected (and is clearly observed in flight experiments [18]). When focusing on the isolated rotor, the resultant modulation due to the harmonic variation in the source–receiver distance and convective amplification effect must be strongest *within* the rotor disk plane ($\theta = 0°$). Later on, it will be shown that this is not the case (Sec. III.B); instead, the change in directivity patterns of the rotor-induced noise, due to changes in operating conditions, is the primary factor influencing BPFM (at least for the low-Reynolds-number rotors considered in this study).

It is important to realize that BPFM does not affect an ensemble-averaged spectrum (or any other second-order statistic). However, the intensity variations are audible, even when the BPF is inaudible to the human ear (this is the case especially for large-scale rotorcraft systems for which typically $f_b < 20$ Hz). Preserving the temporal dimension of the data can be done explicitly by performing a time-frequency analysis. By way of a wavelet transform using a Morlet wavelet, a wavelet power spectrum (WPS) of a noise signal can be generated. Such a time-frequency representation of the acoustic energy is shown in Fig. 2a for a time series that is subject to BPFM (details of the implementation can be found in [34]). Alongside, in Fig. 2b, the ensemble-averaged Fourier spectrum and time-averaged WPS are shown for this stationary noise signal. Note that the Morlet wavelet has a relatively high temporal resolution–at the expense of a fine spectral resolution–with a small cone-of-influence (COI) region. With sufficient resolution in time, it is evident that the noise at $f > 10f_b$ exhibits a strong intensity modulation with a time scale equal to that of the blade passages (indicated by the alternating attenuation and intensification of acoustic energy). It is important to mention that the degree of BPFM noticeable to an observer is dependent on the spectral scale separation and thus the frequency of the modulating signal (e.g., the BPF) relative to the dominant frequency of the carrier signal. As such, it is expected that BPFM will become more relevant for rotors with a lower blade count. An in-depth route to separate tonal and broadband components is also useful to explore (particularly when harmonics appear at very high frequencies). In this regard, cyclostationary spectral analysis [35], wavelet-based methods [36], or semi-empirical fits [37] can be considered, but these are beyond the scope of the current paper.

B. Present Contribution and Outline

In this study, the time- and/or ensemble-averaged characterization of rotor noise is augmented by utilizing metrics that preserve the temporal variation in the intensity of high-frequency noise [38]. This intensity variation is a nonlinear frequency interaction and refers, in the context of our current work, to the phase consistencies between the low-frequency BPF and higher-frequency noise. The underlying

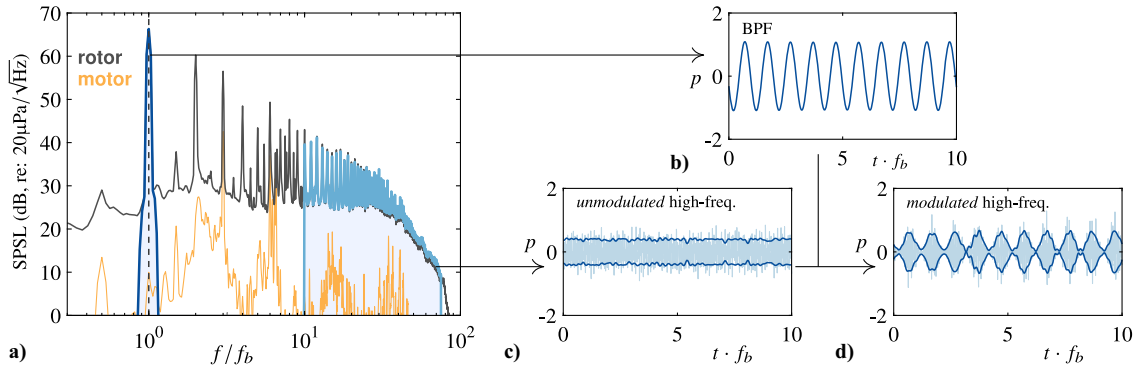

Fig. 1 a) Acoustic spectrum of rotor noise to illustrate BPF modulation (BPFM). b–d) Time series of the narrow band-pass-filtered signal encompassing the BPF, and the high-pass-filtered (un)modulated noise.

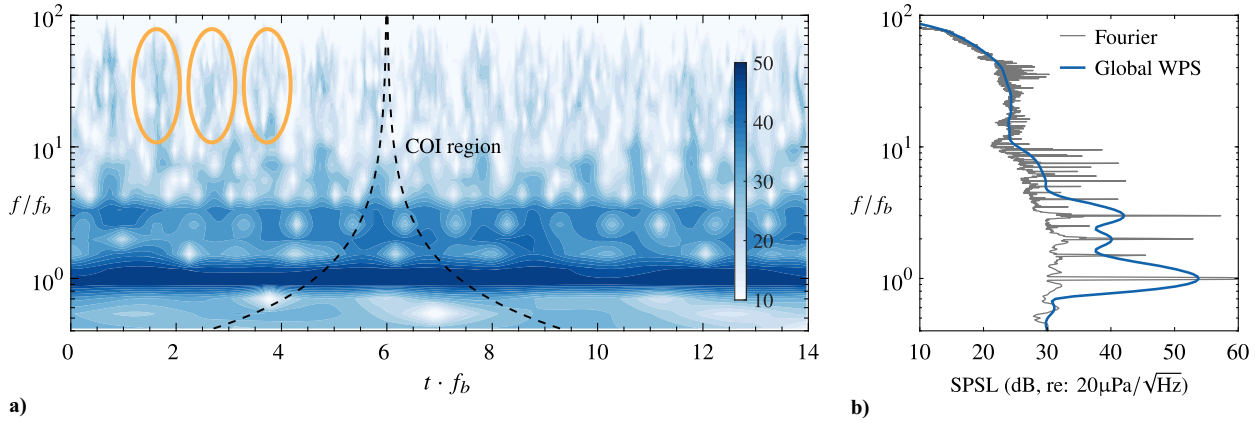

Fig. 2 a) WPS of a rotor noise time series, corresponding to a case with relatively strong BPFM. b) Global, time-averaged WPS corresponding to subfigure (a), compared to a conventional Fourier-based spectrum.

source mechanisms of BPFM are examined through a fundamental study on a fixed-pitch (benchmark) rotor operating with a fixed rotational speed. BPFM is examined for a range of advance ratios (e.g., increments in the incoming freestream velocity), corresponding to a range of loading conditions for the fixed-pitch rotor. Through this study, we intend to contribute toward new measurement and post-processing procedures to support noise regulations and the assessment of the noise impact on communities [39,40].

This paper starts by describing the aeroacoustic experiment of a laboratory-scale rotor (Sec. II). Then, Sec. III covers a brief review of quantifying BPFM, after which directivity patterns of BPFM are presented in tandem with the results of the rotor's inflow disturbances. Since certain noise sources become more (or less) dominant with variations in the advance ratio [29], due to the changing separated flow features around the blade at relatively low Reynolds numbers, these data allow for identifying the source mechanisms responsible for BPFM, which are described in Sec. IV.

II. Experimental Data of a Small-Scale Rotor

A. Experimental Setup and Rotor Operating Conditions

Two experimental campaigns were conducted: 1) acoustic measurements in the rotor's near- and far-field regions, and 2) flowfield measurements using particle image velocimetry (PIV).[‡] All aeroacoustic measurements were conducted in the anechoic A-Tunnel [41] of the Delft University of Technology. This facility is anechoic at frequencies above 200 Hz. Internal dimensions are roughly 6.4 m (L) × 6.4 m (W) × 3.2 m (H). The wind tunnel inlet measures 0.6 m in diameter and provides a uniform, low-turbulence-intensity inflow velocity. For the nominal freestream operating conditions corresponding to nonzero advance ratios of the rotor ($U_\infty \gtrsim 9.6$ m/s), the turbulence intensity defined as $\sqrt{\overline{u^2}}/U_\infty$ is less than 0.1% and around 0.06% for the highest freestream velocity of $U_\infty \approx 24$ m/s. These turbulence intensity levels were obtained from velocity time series acquired using hot-wire anemometry for facility characterization [41]. Time series were filtered in postprocessing using a digital band-pass Butterworth filter of third order. The final turbulence intensity levels quoted above were relatively invariant with changes of the lower frequency bound from 5 to 20 Hz, and totally invariant when changing the bound from 20 to 40 Hz (while keeping the upper bound equal to 20 kHz). Low-frequency turbulence scales of $f \lesssim 5$ Hz still contained negligible energy and do not affect our results due to their quasi-steady nature in the context of the typical BPF of the rotor (262 Hz). Atmospheric pressure and temperature were nominally $p_\infty = 1002$ hPa and $T_\infty = 297$ K, respectively, throughout the measurement duration (with only slight variations in the temperature to within ±1K). These values yield a density of $\rho_\infty = 1.180$ kg/m^3 and a sound speed of $a_\infty = 345.5$ m/s. Relative humidity was inferred from an indoor weather station and equaled RH = 40%. Atmospheric conditions are used in correcting the acoustic data for atmospheric absorption (Sec. II.B), even though this correction is minor due to the relatively small propagation distances.

A rotor test rig was mounted to the circular wind tunnel inlet, supporting a small-scale rotor in hover. A circular nacelle of 5 cm in diameter embedded a compact 6-axis ATI Mini40 sensor (with maximum thrust and torque capacities of 40 N and 1 N·m, respectively), providing rotor thrust and torque readings. An LMT 2280 brushless motor was used in combination with a TDK-Lambda power supply to drive the rotor, comprising a voltage range of 0–60 V and a current range of 0–80 A. A US Digital EM1 transmissive optical encoder, coupled with a US Digital disk of 25 mm in diameter, gave a one-per-revolution (1P) signal of the rotor shaft for a reading of its rotational speed and angular position. The induced flow direction was physically upward in the facility, but in all plots the orientation is flipped upside down to represent a rotor-in-hover scenario when $J = 0$. Finally, it is important to mention the effects of possible flow recirculation in the anechoic facility. Previously, for rotors in hover, flow recirculation in a closed anechoic chamber has been linked to an intensification of BPF harmonics in the sound pressure spectrum level (SPSL) [42,43]. Casalino et al. [44] simulated the facility used in the current study and showed that the anechoic chamber confinement has no influence on the acoustic spectra and flow features on the rotor blades for a nonzero advance ratio. Only for the $J = 0$ case it was concluded in [44] that BPF harmonics in the acoustic spectra had a larger amplitude when confinement was present. They verified that when auto-induction was included correctly in the simulation (even though recirculation was absent), the experimental results were replicated. It is unsure whether recirculation effects are totally absent in our experimental study with the relatively large (anechoically treated) exhaust slit located ≈$6D_p$ downstream of the rotor (Fig. 3c). However, even if BPF harmonics are intensified due to turbulence impingement—in addition to the leading-edge BWIs that already appear in hover—we expect our conclusions to be unaffected since analyses of BPFM rely on energy-normalized metrics (Sec. III.B).

The rotor itself was derived from an APC propeller (model 9x6e); this rotor has a diameter of 9 inches. For the current setup, the diameter was scaled up to $D_p = 2R = 0.30$ m, while all blade elements were reshaped with a NACA 4412 airfoil. Final distributions of the chord and twist (pitch) angle of the blade as a function of the radial distance from the hub center, are reported by Grande et al. [29], who used the exact same rotor. The rotor, made of an aluminum alloy, was manufactured in-house using CNC machining; a surface finish of the rotor blades was achieved with a roughness average (Ra value) of 0.4–0.8 μm. This rotor is identical to the one used in benchmarking studies (i.e., BANC X), focusing on the flow transition over the blades and its influence on the aeroacoustic performance [29,30,45]. The rotor spun at a nominal rate of $\omega = 131.0$ rev/s (7860 rotation per minute [RPM]), resulting in a BPF of

[‡]All acoustic data are available online through open-access publishing: https://doi.org/10.4121/9c8cf649-7617-42e2-a9b1-a32d5f483964. Flow-field data are available upon request: please email the authors at w.j.baars@tudelft.nl.

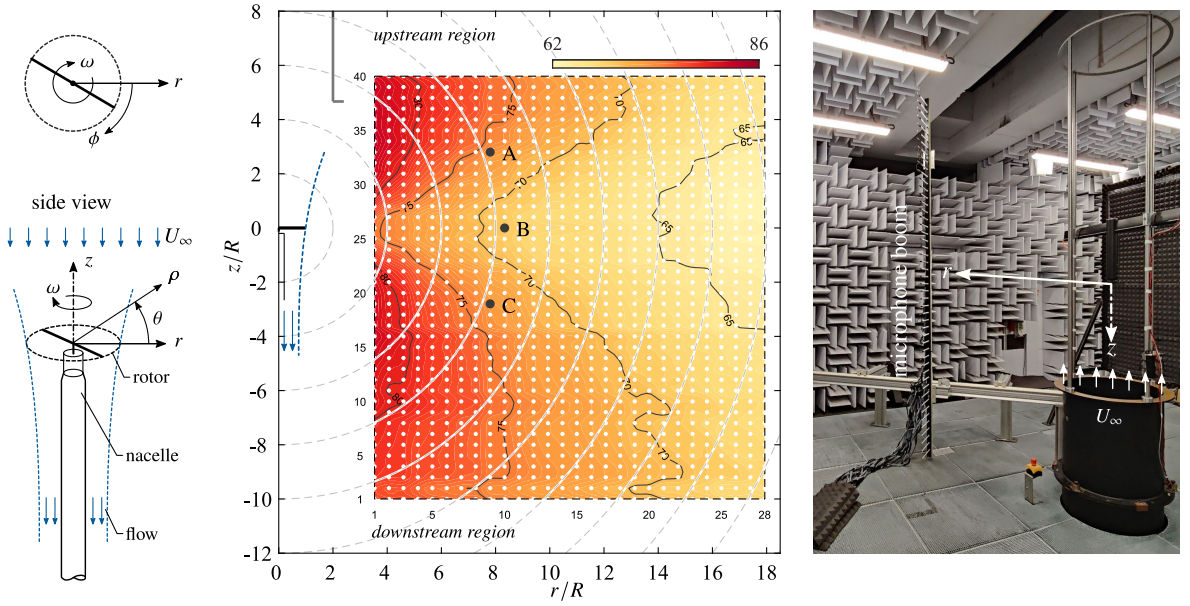

a) Top view **b) Acoustic grid & high-pass filtered noise ($J = 0$)** **c) Setup inverted in z**

Fig. 3 a, c) Schematic and photograph of the experimental setup. b) Acoustic grid of 1120 microphone positions mapped out with a linear microphone boom; the acoustic contour is described in the text.

$f_b = 262.0$ Hz. Rotor rotational speed was kept constant to within $\pm 0.1\%$ with the aid of a closed-loop PID-type controller working with the 1P signal. For the hover condition, the Reynolds number was $Re_{c75} \equiv c_{75} 2\pi\omega 0.75R/\nu = 1.35 \cdot 10^5$, based on the blade chord of $c_{75} = 22.4$ mm at $r = 0.75R$, and the tip Mach number was $M_{\text{tip}} \equiv 2\pi\omega R/a_\infty = 0.358$ (note that the rotational speed of the rotor in rad/s is denoted as $\Omega = 2\pi\omega$). Predicting the noise can be difficult at low Reynolds numbers [45–48], when the rotor operates with a reduced efficiency. Hence, the experimental data can aid in the validation of simulations and auralization efforts of low-Reynolds-number rotor aeroacoustics.

To consider a variation in rotor blade loading (as a representation of varying forward flight velocity with fixed RPM rotors), various advance ratios were considered. The advance ratio is defined as $J \equiv U_\infty/(\omega 2R) = \pi U_\infty/U_{\text{tip}}$, and four different values were considered by fixing the rotational speed of the rotor, while changing the tunnel inflow (freestream) velocity U_∞. A total of four advance ratios are considered, where $J = 0$ (hover), 0.24, 0.41, and 0.61. The reason for these values becomes clear later on when discussing the rotor operating performance. The four advance ratios considered correspond to freestream velocities of $U_\infty \approx 0$, 9.6, 16, and 24 m/s, respectively. Tip Mach numbers and Reynolds numbers were nearly constant (listed in Table 1) and are based on a total velocity, composed of the rotor's rotational speed component and the incoming freestream velocity component (e.g., $M_{\text{tip}} = U_{\text{tip}}/a_\infty$, with $U_{\text{tip}} = \sqrt{(\Omega R)^2 + U_\infty^2}$). Measurements of the thrust force (F_z) and rotor torque (τ_z) were performed for each advance ratio to yield rotor-performance data (Table 1). The coefficients of thrust (C_T) and torque (C_τ) and the propulsive efficiency (η_p) were calculated following the relations

$$C_T = \frac{F_z}{\rho A \Omega^2 R^2}, \quad C_\tau = \frac{\tau_z}{\rho A \Omega^2 R^3}, \quad \eta_p = \frac{J C_T}{\pi C_\tau} \tag{1}$$

Here $A = \pi R^2$ is the rotor disk area; rotor power in watts is taken as $P = \Omega \tau_z$. Finally, for the hover condition only, the rotor's figure of merit (FM) was computed following the conventional definition

$$\text{FM} = \frac{C_T^{3/2}}{\sqrt{2} C_\tau} \tag{2}$$

Thrust and torque coefficients, as well as the propulsive efficiency, are functions of the advance ratio and are compared to the literature in Fig. 4. Data from the literature (black symbols) considered the same rotor and facility, except for lower rotational frequencies. As such, our current measurements also considered a lower rotational frequency for a direct comparison ($\omega \approx 66$ Hz, with the open red markers), and these data match well with the literature. At the higher rotational speed considered in this paper (solid red markers), the rotor operates at a higher thrust coefficient as the consequence of a more turbulent (slightly less separated) flow; this comes at the expense of a larger torque coefficient, although the propulsive efficiency remains equal.

At hover, the thrust and torque coefficients can be compared to a parametric study on small-scale rotors by Tinney and Sirohi [6]. Even though the FM is equal, our thrust and torque coefficients are higher by about 30 and 40%, respectively. This is presumably caused by the more aggressive pitch of the rotor blades (roughly twice as high in the current study). When considering nonzero advance ratios, the thrust coefficient is known to decrease with an increase in J, due to the lower rotor disk loading. The torque coefficient stays roughly constant for

Table 1 Operating conditions of the $D_p = 0.30$ m diameter rotor, for each of the four advance ratios J

	Rotor operating parameters				Rotor performance metrics						
Case J	U_∞, m/s	f_b, Hz	M_{tip}	Re_{c75}	F_z, N	τ_z, N·m	P, W	$C_T \cdot 10^2$	$C_\tau \cdot 10^3$	η_p	FM
0	0	262.0	0.358	$1.36 \cdot 10^5$	21.3	0.41	339	1.66	2.14	0	0.70
0.24	9.6	262.0	0.359	$1.36 \cdot 10^5$	17.9	0.44	361	1.39	2.28	0.48	— —
0.41	16.0	262.0	0.361	$1.38 \cdot 10^5$	14.0	0.41	341	1.09	2.15	0.66	— —
0.61	24.0	262.0	0.365	$1.40 \cdot 10^5$	8.3	0.41	253	0.65	1.60	0.78	— —

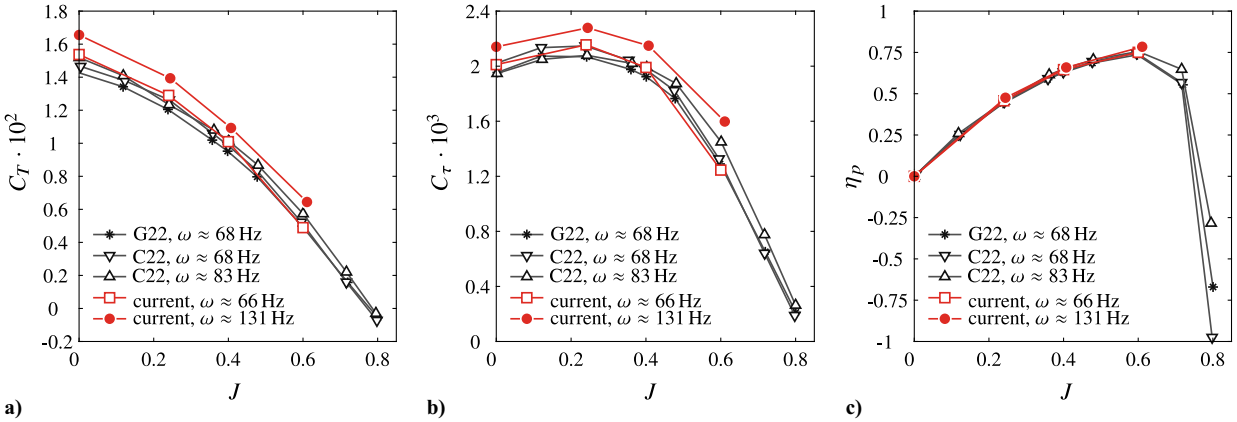

Fig. 4 Rotor performance data: a) thrust coefficient, C_T, b) torque coefficient C_τ, and c) propulsive efficiency η_p as a function of the advance ratio J. Current performance data are compared to the literature (G22: Grande et al. [29] and C22: Casalino et al. [48]).

$J < 0.4$ due to the separated flow close to the root of the blades, resulting in large drag values, as reported by Grande et al. [29]. The propulsive efficiency does increase with J [3,29], since the blade section's angle of attack reduces and the torque decreases sufficiently fast so that the rotor efficiency peaks at $J \approx 0.6$ (these studies considered $\omega \approx 67$ rev/s, but the performance trends are evidently similar for our current rotational speed of $\omega \approx 131$ rev/s). The four advance ratios that are currently being considered were chosen to span the range in propulsive efficiencies from a hover condition up to its maximum value near $J = 0.6$ (Fig. 4c). This sweep in advance ratios of the rotor (with uniform inflow, e.g., the rotor disk plane is always perpendicular to the incoming flow) ensures the presence of different flow features encountered in fundamental propulsive rotor aerodynamics at low Reynolds numbers. These flow features will be discussed further in Sec. IV when interpreting results, but will include phenomena such as BWI at $J = 0$, and the appearance of laminar separation bubbles and an enhanced vortex shedding by its shear-layers at higher advance ratios.

B. Measurements of the Acoustic Field and Rotor-Induced Flowfield

Acoustic data were acquired using a linear microphone boom with 40 sensors ($m = 1{:}40$ microphone positions, see Fig. 3b), comprising an equidistant spacing of 60 mm. The vertical boom was mounted to a horizontal beam so that it could be traversed in r. Free-field microphones were oriented such that their measuring diaphragms were coplanar with the measurement plane (this orientation avoids having to point the normal vector of the diaphragm to an aeroacoustic sound source location that can be ambiguous [49,50]). A free-field microphone correction was applied in all spectral analyses to account for the intrusive nature and form factor of the microphone (90° grazing incidence waves), although it only marginally affects the intensity at $f > 10$ kHz. For each advance ratio J, the acoustic field was mapped out by translating the microphone boom to 28 radial positions ($b = 1{:}28$ boom positions, see Fig. 3b) with traversing steps of 80 mm, resulting in a total of $28 \times 40 = 1120$ positions for which pressure time series $p(r, z; t)$ are available (see Fig. 3b).

The sensors used were 1/4in. free-field microphones (GRAS 40PH), with a frequency response range of 5 Hz to 20 kHz with a ± 2 dB accuracy (and a ± 1 dB accuracy from 50 Hz up to 5 kHz) and with a dynamic range of 32 A-weighted dB level (dBA) to 135 dB, with a sensitivity of 50 mV/Pa. Microphones were calibrated in situ with a GRAS 42AA piston phone. All 40 microphones were IEPE-powered and simultaneously sampled with several NI PXIe-4499 sound and vibration modules (onboard filtering before digitization with a 24-bit accuracy). All signals were sampled at a rate of $f_s = 51.2$ kHz for a duration of $T = 40$ s ($2T\omega \approx 10480$ blade passages); this was confirmed to be more than sufficient for converged bispectral statistics at the lowest frequency of interest (see [51] and the Appendix). For spectral-based analysis, the one-sided spectrum is taken as $\phi_{pp}(r, z; f) = 2\langle P(r, z; f)P^*(r, z; f)\rangle$, where $P(r, z; f) = \mathcal{F}[p(r, z; t)]$ is the temporal Fast Fourier Transform (FFT) and $\langle\cdot\rangle$ denotes ensemble averaging. An SPSL in dB follows from $\mathrm{SPSL}(r, z; f) = 10\log_{10}(\phi_{pp}(r, z; f)/p_{ref}^2)$, with $p_{ref} = 20\ \mu\mathrm{Pa}/\sqrt{\mathrm{Hz}}$. Ensemble averaging was conducted using FFT partitions of $N = 16f_s/\omega$ samples to ensure that the discrete frequencies align with the BPF and its harmonics; this reduces the leakage of tonal energies into neighboring frequencies [6]. The value of N yields a spectral resolution of $df = 8.2$ Hz and 653 ensembles with 50% overlap.

For all analyses, the raw pressure time series were subjected to a band-pass filter with a flat response between 60 Hz and 15 kHz, suppressing the nonanechoic, low-frequency content and the energy beyond the highest frequency range of the microphone. The SPSL was also corrected for atmospheric absorption (ANSI S1.26-1996) with an assumed propagation distance from the rotor hub (primarily affecting $f > 10$ kHz). In addition, an A-weighting was applied (ANSI S1.6-1967) to account for the relative loudness perceived by the human ear [52] and attenuates energy at $f \lesssim 3f_b$. Note that the conclusions of this paper are unaffected by applying the A-weighting since the BPFM is studied through normalized metrics. Sound refraction through the shear layer of the open jet wind tunnel was not considered [53], since corrections are negligible (the highest freestream velocity yields a convective Mach number of less than ≈0.07, and propagation distances through the convective flow are small). Finally, it was confirmed that motor-only noise was far less intense than the rotor noise. As an example, the acoustic pressure spectra shown in Figs. 5a and 5b correspond to microphone B, for $J = 0$ and 0.41, respectively. Raw and corrected pressure spectra of the rotor noise are shown, as well as the corrected noise spectra of only the motor (spinning without rotor but at the same RPM) and the noise floor of the facility (with only the wind tunnel running for the $J \neq 0$ cases). The noise of the rotating motor alone has the expected spectral peak at $f = \omega = f_b/2$ and is also relatively dominant in the vicinity of $f = 14\omega = 7f_b$, which is caused by the 14 magnetic poles of the motor (motor noise is also known to arise from structural vibrations and harmonic interference [54,55]). Overall, the magnitudes of the noise floor and motor noise are lower than the rotor noise. Though, note that the motor noise corresponds to an unloaded case (a spinning shaft), which can change the noise intensity in comparison to the loaded case (the degree of which is unknown).

Flowfields were captured using a stereoscopic PIV setup (Fig. 6) that is similar to the one reported by Grande et al. [29,30]. With a double-cavity Quantel Evergreen EVG00200 Nd:YAG laser, a sheet was created to illuminate a relatively large region on one side of the rotor axis. Our current PIV field of view (FOV) aids in detailing the vortical flow structures in the near vicinity of the rotor blade. Two Imager sCMOS cameras were used with 2560×2160 px^2. Two Nikon lenses were mounted with Scheimpflug adapters, each with a 60 mm focal length and an f# of 11. In this work, we only consider 500 image pairs that were acquired in a phase-locked sense using the 1P signal. A sample result of the PIV campaign is shown in Fig. 6b and is described in the caption.

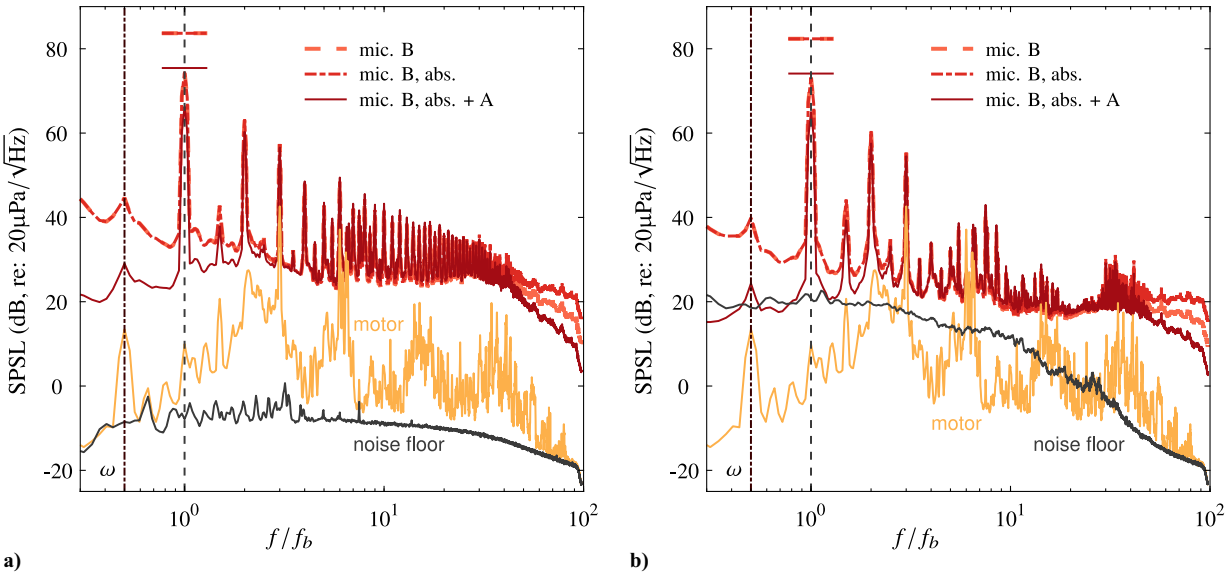

Fig. 5 Acoustic spectra for a) $J = 0$ and b) $J = 0.41$, corresponding to microphone B (indicated in Fig. 3b). SPSL magnitudes of the BPF (horizontal bars) are described in the text.

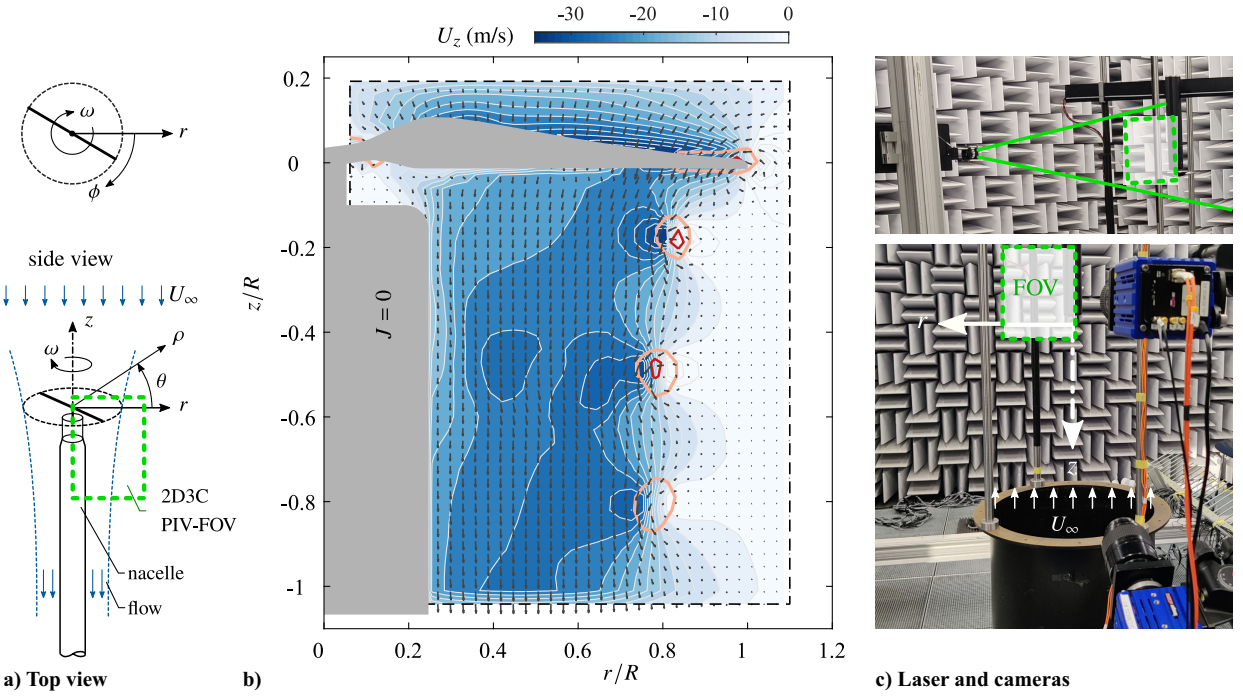

Fig. 6 a, c) Setup with the PIV field of view. b) Contour of the phase-averaged vertical velocity U_z at a near-zero phase angle behind the blade for $J = 0$; vectors show the in-plane velocity with a vector skip of 15. Superimposed are two red isocontours of in-plane vorticity at magnitudes of $\omega_\phi = 1500$ s^{-1} and 7500 s^{-1}.

C. Sound Pressure Level Statistics

The basic features of the acoustic data are documented here to generate an appreciation of the different noise characteristics of the rotor with the varying advance ratio J. For brevity, the case of $J = 0$ is chosen to present a few intermediate results. First, recall that a spatial topography of the integrated SPSL over $f > 10f_b$ was shown in Fig. 3b. The SPL of this integrated, high-pass-filtered noise content is referred to as $\bar{p}_{10f_b}$, and its spatial contour clearly illustrates that the higher-frequency broadband noise exhibits the well-known quadrupole directivity pattern [25,56]. Throughout the remainder of the paper, the $f > 10f_b$ range is used in defining the high-frequency noise content. Changes in the $10f_b$ threshold do not affect the conclusions made. The acoustic data can be condensed to directivity arcs for ease of interpretation: SPSL statistics corresponding to all 1120 measurement points were projected to a rotor-hub-centered[§] arc with a virtual radius of $\rho = 5D_p$. In this projection, a spherical spreading law was adopted, according to $p \propto 1/\rho$. Thus, a data collapse would imply that all measurement points were located in the acoustic far field. The results for $\bar{p}_{10f_b}$ are presented in Fig. 7c, showing a rather excellent collapse of the data. This is further accentuated with the set of three lines (solid, dash-dotted, and dashed), resulting from a fit to the projected data from the three most outward upper–vertical–lower perimeters of locations spanned by the microphone grid, respectively. Variations are less than ≈1 dBA, and

[§]Since the noise is, on average, emitted from the center location of the spinning rotor blades, this hub-centered source position resulted in the best collapse of the data in Figs. 7b and 7c.

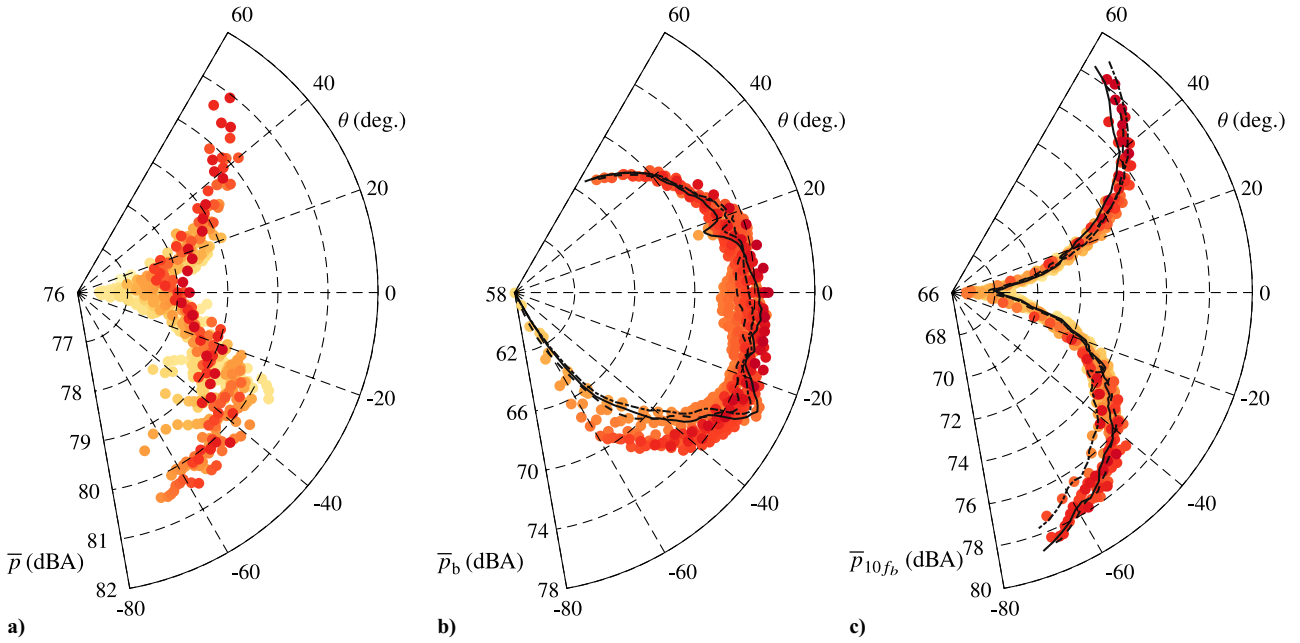

Fig. 7 Noise directivity patterns for advance ratio $J = 0$, obtained via spherically projecting the 1120 data points to a rotor-hub-centered arc of radius $\rho = 5D_p$. Subfigures correspond to the a) OASPL, b) SPSL of the BPF, and c) integrated SPSL over $f > 10f_b$ (points are colored per the unprojected noise levels).

these variations are more pronounced for large angles θ, for which the microphones on the vertical boom were relatively close to the walls of the anechoic chamber. Withal, collapse of $\bar{p}_{10f_b}$ data is expected: the source of these frequencies is acoustically compact, since the wavelength corresponding to $10f_b$ is $\lambda/D_p = a_\infty/(10f_b)/D_p \approx 0.43$, and all microphone locations were situated far from the rotor's hub ($r/R \gtrsim 4$), except for the closest measurement points at a region around $\theta = 0°$. Hence, this is the angle at which the collapse of the data markers in Fig. 7c is least good.

When performing the same data-projection procedure for the overall sound pressure level (OASPL; integral of the spectra over the entire frequency range), we obtain the directivity shown in Fig. 7a. The absence of collapse suggests that some locations, in terms of the OASPL, were not yet situated in the acoustic far field. When considering the SPSL of only the BPF,[¶] and performing again a spherical projection to a virtual arc with a radius $\rho = 5D_p$, we obtain the SPL denoted as $\bar{p}_b$ (Fig. 7b) in dBA. Rotor-thickness noise is classified as an acoustic monopole source, while the loading noise from thrust and torque radiates according to an acoustic dipole source. Loading noise is thus strongly confined to a region around the rotor plane, but for the thrust-producing rotor the maximum noise intensity is oriented slightly toward the downstream direction. Since the BPF has an acoustic wavelength of $\lambda/D_p = a_\infty/f_b/D_p \approx 4.3$ and is not acoustically compact, only a subset of data points lie within the acoustic far-field of the rotor at this frequency.

Noise directivity patterns of $\bar{p}_b$ and $\bar{p}_{10f_b}$ are now generated for all four advance ratios J, following the same procedure as described above for $J = 0$. In order to visualize the result, only the curves found through a fitting procedure to the projected data from the most far-field locations are considered. Again, these fits are done to the three most outward upper–vertical–lower perimeters of locations spanned by the microphone grid. Results are shown in Figs. 8a and 8b for the BPF content and high-frequency noise, respectively. Two primary trends are observed. Firstly, the BPF tone reduces in amplitude due to the lower intensity of the loading noise (an increase in advance ratio causes a direct decrease in disk loading). Secondly, the high-frequency noise reduces in overall amplitude too, but does not exhibit a monotonic decrease with an increase in J. That is, the high-frequency noise content decreases for $J = 0 \rightarrow 0.24 \rightarrow 0.41$, but then increases again for the highest advance ratio of $J = 0.61$. This complex behavior is related to noise sources associated with the change in separated-flow features over the blade [29,30,48]. With increasing J, the separation goes from a fully laminar separation ($J = 0$), to one that reattaches and forms a laminar separation bubble ($J = 0.24$ and 0.41), to one that fully separates in a turbulent state ($J = 0.61$). For the latter case, the trailing-edge noise is more intense than for the laminar separation, resulting in an increase in noise intensity compared to the two intermediate advance ratios. The reason why the high-frequency noise is so dominant for the $J = 0$ case (recall the magnitude of the directivity pattern shown in Fig. 7c) is because of the occurrence of BWI (in which the blades encounter an imprint of the blade wake and tip vortex deployed by the consecutive blade).

Finally, this section merely illustrates that acoustic data of sufficient quality were taken in both the acoustic near and far fields. Note, however, that the BPFM analysis of Sec. III is unaffected by the pressure obeying (or not obeying) a far-field amplitude decay rate. Specifically, the modulation metrics are correlation-based and energy-normalized.

D. Flowfield in the Blade's Near-Vicinity

The results of PIV reveal the primary flow features induced by (and encountered by) the rotor blades. Phase-locked fields of various flow quantities at a near-zero phase angle behind the blade are shown in Fig. 9, for all four advance ratios J. Fields of the in-plane vorticity ω_ϕ are shown in Figs. 9a–9d. The locations of the tip vortices are well-identified, as well as the vorticity in the wake sheet of the blade. For the three nonzero advance ratios, this blade wake connects the tip vortex at a wake age of 180° to the rotor hub where a relatively weak root vortex folds around the nacelle. For the $J = 0$ case, the tip vortices and wake sheets have a small axial spacing, causing an interaction of the wake sheets associated with the 180° and 360° wake ages (as described by Thurman and Baeder [57]). As expected for lower blade loading, the vorticity magnitude decreases with an

[¶]Here, the SPSL magnitude is taken as the root-mean-square amplitude of a time series resembling the *pure* BPF tone, as was shown in Fig. 1(c), where $A/\sqrt{2}$ is a harmonic wave with amplitude A. By computing the SPSL magnitude this way, instead of taking the peak of the spectrum at $f = f_b$, it is ensured that the magnitude is *independent* of the chosen spectral resolution df. In practice, the amplitude is obtained by taking the magnitude of $\mathrm{SPSL}_{\mathrm{tone}}(r, z; f) = 10\log_{10}(\phi_{\mathrm{pp}}(r, z; f)df/p^2_{\mathrm{ref}})$ at $f = f_b$. Note that here ϕ_{pp} is premultiplied by df: this yields an unambiguous value for the BPF peak amplitude and hence the subscript "tone."

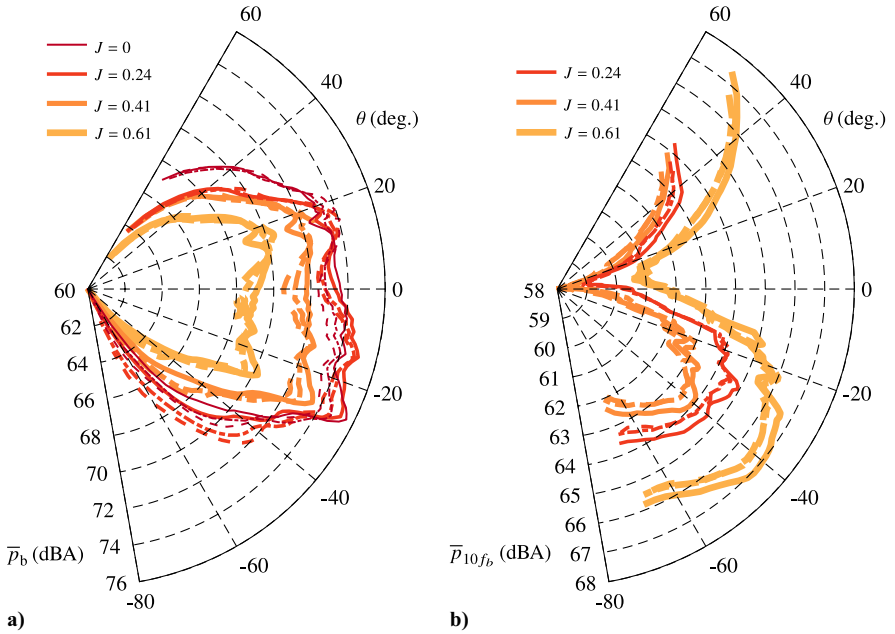

Fig. 8 Noise directivity patterns, as per Figs. 7b and 7c, but now for all four advance ratios J. Each set of three lines (solid, dash-dotted, dashed) resembles a fit to the projected data (see text). For subfigure (b), the directivity pattern of $J = 0$ is omitted to keep the radial scale condensed ($J = 0$ was shown in Fig. 7c).

increasing value of J. Figures 9e–9h and 9i–9l show filled contours of the horizontal velocity U_r (positive outboard) and vertical velocity U_z (negative downward). Superimposed on these two sets of plots are two isocontours of the in-plane vorticity, ω_ϕ, to highlight the location of the tip vortices. It becomes apparent that the vortical flowfield leading to the onset of the tip vortex causes an inboard motion of the flow on the blade's suction side and outboard on the blade's pressure side. For $J = 0$, the inboard horizontal velocity reaches more than 10% of the rotor-tip velocity. This high velocity magnitude is the consequence of the contracting slipstream and an inboard flow induced by the preceding blade's tip vortex, situated with its core less than $0.2R$ below the rotor plane. For this zero advance ratio case, the noise generated by this BWI has a leading-edge noise production mechanism. Evidence for this is shown in the acoustic spectra of Fig. 5: the spectrum for $J = 0$ includes a multitude of harmonics in the midfrequency range around $f/f_b = 10$. This is indicative of leading-edge scattering and thickness noise components determined by the interaction of the blade with the turbulent flow in the previous blade's wake. The physics of the interaction mechanism has been reported in the works by Sevik [58] and Hanson [59], and a more detailed description using the wavelet method is presented for $J = 0$ for the same benchmark rotor in the recent work by Meloni et al. [36]. The tonal noise is less strong in the cases of nonzero advance ratios (this will also be clear from the acoustic spectra presented later on). Even for the $J = 0.24$ case, the tip vortex with a 180° wake age trails relatively close to the pressure side of the blade, and an imprint of this vortical flow still appears clearly at the bottom edge of the blade near $r/R \approx 0.6$. Only for $J \geq 0.41$, the influence of the vortical flow from the preceding blade no longer affects the flow around the successive blade in terms of a horizontal velocity disturbance in the phase-locked mean field. Finally, see Grande et al. [30] for detailed PIV-based velocity fields in the cross-section of the blades at $r/R = 0.6$.

III. Blade Passing Frequency Modulation

A. Phase-Averaged Acoustic Signature

A first method to assess BPFM is to use phase-averaged pressure data, denoted as $\tilde{p}(r, z; \tau)$, with τ being the time coordinate within one full rotor revolution. Signatures of the phase-averaged pressure are shown in Fig. 10. For each J, we show the phase-averaged pressure time series for 1) the BPF tone $\tilde{p}_b$ and 2) the phase-averaged pressure in the absence of the BPF (thus $\tilde{p} - \tilde{p}_b$, with the red thick line). Since microphones A, B, and C are located at the same radial distance ρ (Fig. 3b), the time series of the BPF are nearly identical at all three locations. Signature $\tilde{p} - \tilde{p}_b$ is the resultant of the second- and higher-order harmonics being phase-consistent with the BPF, thus surviving the phase average. The finer undulations within the signal (for instance, clear in the mic. B signal in Fig. 10b) correspond to roughly the seventh harmonic (postulated to be motor noise as discussed earlier). By construction, the signature does not contain any (phase-inconsistent) broadband noise. Nevertheless, BPFM can still be visualized: in the background of the red curves are 15 ensembles of the raw acoustic pressure, high-pass filtered at $f > 10f_b$. In addition, upper and lower envelopes to the intensity of these raw time series are shown, which were created using a Hilbert transform and by considering all 5240 rotation ensembles. A strong link between the variation in the high-frequency noise intensity and the BPF signal is clearly noticeable. For the signal of mic. C (particularly for $J = 0.24, 0.41$, and 0.61), the intensity variation is well-correlated to the BPF signal, while this correlation is less strong for mic. A.

To visualize BPFM throughout the spatial extent captured by the acoustic data, similar analyses as the ones performed to construct Fig. 10 can be performed for each microphone. The phase-averaged pressure data allow for creating a spatial contour of $\tilde{p}(r, z; \tau)$ for one specific value of τ (note that movies with temporal evolution, $\tau \in [0, 2f_b)$, are available as supplementary material). Figure 11a shows this contour for the case of $J = 0.41$. Evidently, the BPF is dominant with a spatial wavelength of around $4.3D_p$; finer undulations superimposed on the BPF are also visible, as well as the decaying nature of the sound wave amplitude. Alongside, in Fig. 11b, a contour is shown of the envelope amplitude to the intensity of the high-pass-filtered signal at $f > 10f_b$ (thus visualizing a spatial variation of one temporal instant of the envelope signals shown in Fig. 10). This contour of the envelop amplitude is presented with a zero mean: the mean value of the envelope function was subtracted before plotting the contour (thus, a positive value of the contour means that the intensity of the high-pass-filtered signal p_{10f_b} is higher than the mean intensity, and vice versa for a negative value of the contour). Certainly below the rotor disk plane, a strong link exists between the BPF signal and the variation in the high-frequency noise. Trends follow Fig. 10c in that the link appears strongest along a radial path going through mic. C, while being weakest for a path going through mic. A. Moreover, the phase shift between the BPF and the envelope changes drastically when moving from locations above the

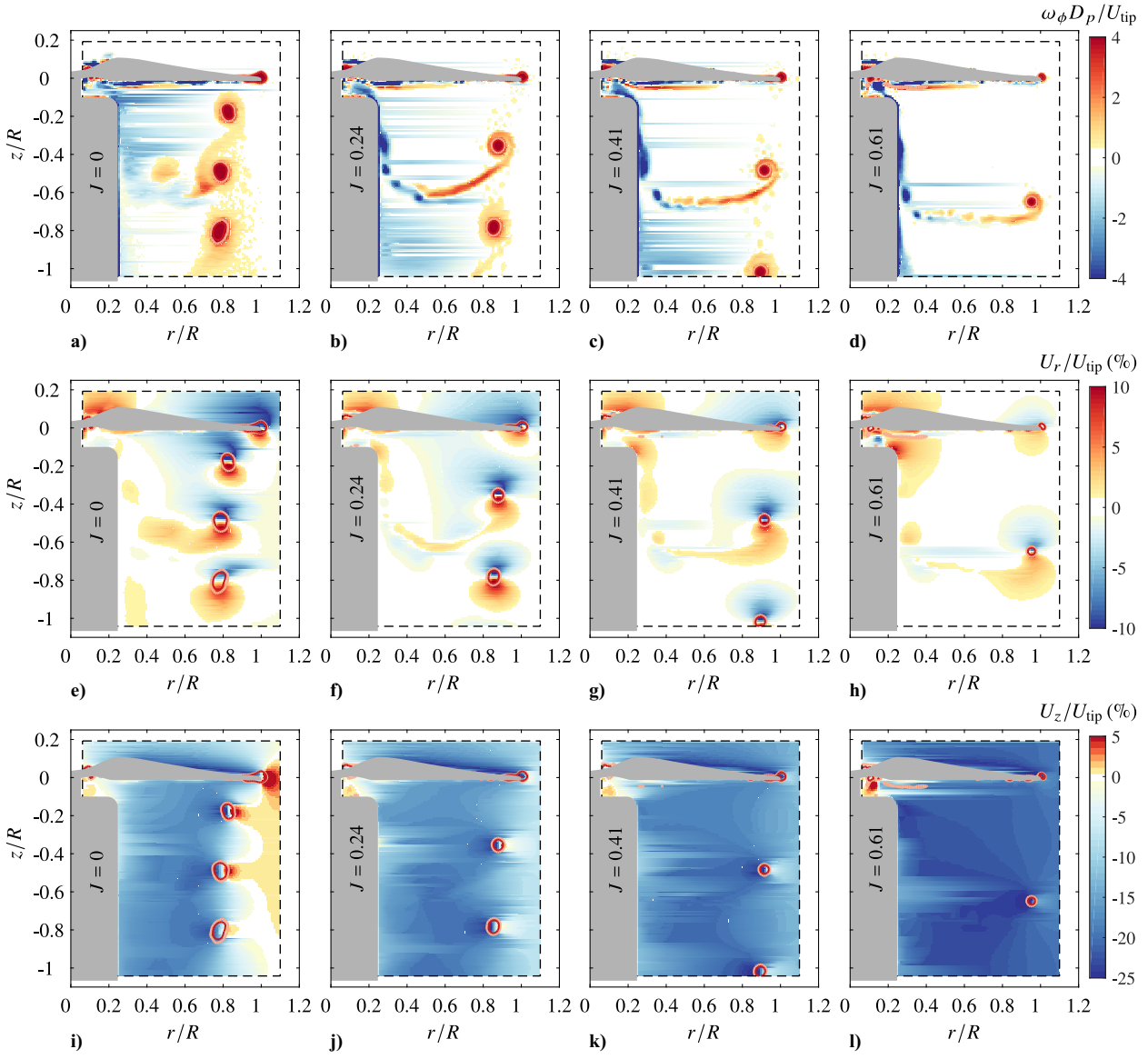

Fig. 9 Filled contours of a–d) in-plane vorticity ω_ϕ, e–h) horizontal velocity U_r, and i–l) vertical velocity U_z, for all four advance ratios J. Superimposed on all plots are two red isocontours of in-plane vorticity ω_ϕ corresponding to normalized vorticity magnitudes of $\omega_\phi D_p/U_{\text{tip}} = 3.5$ and 7.0.

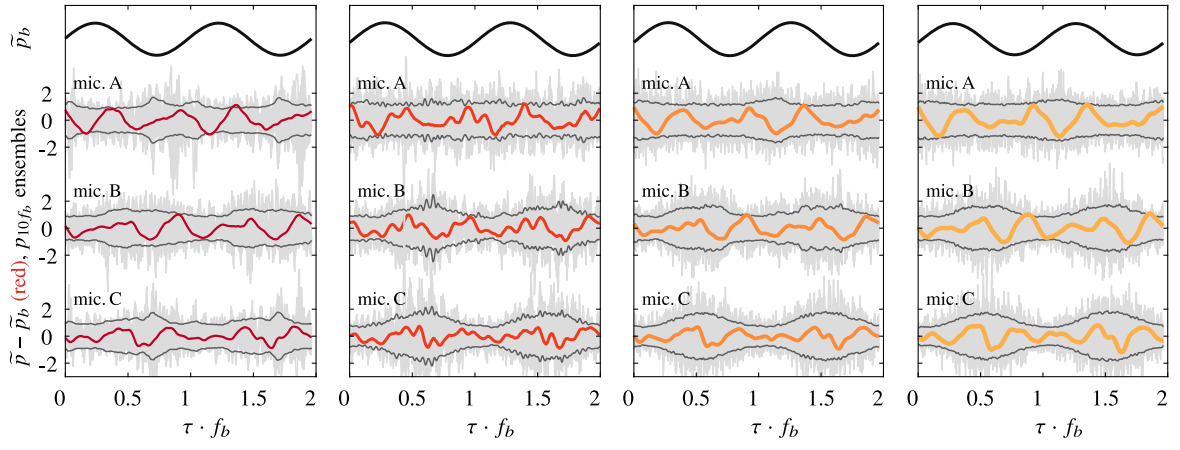

Fig. 10 Phase-averaged acoustic pressure signatures. For all four advance ratios J, from top-to-bottom: BPF tone $\tilde{p}_b$; phase-averaged pressure signal in the absence of the BPF tone, $\tilde{p} - \tilde{p}_b$ (in red); phase-averaged envelope of the high-pass-filtered signal p_{10f_b} (dark gray) and 15 ensembles superimposed (light gray).

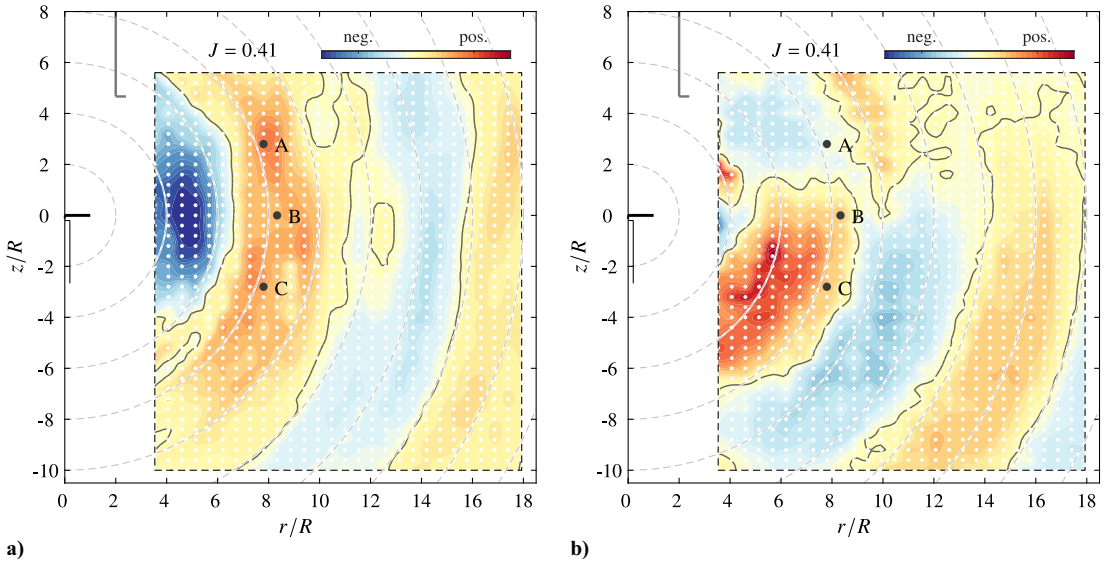

Fig. 11 For the case of $J = 0.41$, spatial topography of a) the phase-averaged pressure signal $\tilde{p}(r,z;\tau)$ for one specific value of τ, and b) the phase-averaged zero-mean envelope of the high-pass-filtered signal p_{10f_b}.

rotor disk plane to ones below it. Next, BPFM will be quantified with correlation-based scalar metrics.

B. Scalar Metrics and Directivity Patterns of Modulation

Baars et al. [38] described methods for quantifying BPFM. The various scalar metrics involved in this process are briefly summarized below, and it must be emphasized that these are computed from a single acoustic pressure time series. Then, the metrics are computed for every acoustic pressure time series of the grid measurements to inspect the directivity trends of the modulation.

i) Through a bispectral analysis, the dominant quadratic interfrequency coupling can be found out of all possible frequency combinations present within a signal. By correlating two frequency components, f_1 and f_2, to their sum ($f_3 = f_1 + f_2$) or difference, this can be expressed as an auto-bicoherence, $\gamma^2_{\mathrm{ppp}}(f_1, f_2)$:

$$\gamma^2_{\mathrm{ppp}}(f_1+f_2) = \frac{|\phi_{\mathrm{ppp}}(f_1,f_2)|^2}{\phi_{\mathrm{pp}}(f_1)\phi_{\mathrm{pp}}(f_2)\phi_{\mathrm{pp}}(f_1+f_2)} \in [0,1] \qquad (3)$$

Here, the numerator is the auto-bispectrum, taken as $\phi_{\mathrm{ppp}}(f_1,f_2) = 2\langle P(f_1+f_2)P^*(f_1)P^*(f_2)\rangle$. Coordinates r and z are omitted for ease of notation. Note that $\gamma^2_{\mathrm{ppp}}(f_1,f_2)$ indicates the degree of normalized correlation between the energy at f_1 and f_2, and the energy at $f_1 + f_2$ (here we only consider sum interactions, and not the difference interactions per $f_3 = f_1 - f_2$, as we are interested in how the low-frequency BPF modulates higher-frequency noise). A sample auto-bicoherence spectrum is shown in the Appendix, corresponding to the time series of mic. C at conditions of $J = 0$ (Fig. A1) and $J = 0.41$ (Fig. A2). Typically, a ridge of relatively strong coherence appears along $f_2 = f_b$, meaning that the BPF is phase-coupled to a broad range of frequencies within the same signal, $f_1 > f_b$. Said quadratic coupling is suppressed in phase averaging (Sec. III.A) because the *phase* in the auto-bispectrum can still vary per triad. A single metric Γ^2_m is constructed by averaging $\gamma^2_{\mathrm{ppp}}(f_1,f_2)$ for the primary frequency $f_2 = f_b$ and all possible quadratic frequency doublets residing at $f_1 > 10f_b$ (details in the Appendix).

ii) The concept of *modulating* and *carrier* signals allows for the application of standard linear correlation methods. The modulating signal $p_b(t)$ is taken as the BPF-associated time series, while a carrier signal $p_h(t)$ is taken as the time series resulting from high-pass filtering at $f > 10f_b$. An envelope capturing the time-varying intensity of the latter signal can be generated through a Hilbert transform $\hat{p}_h(t) = |H[p_h(t)]|$. By correlating the modulating signal $p_b(t)$ with the carrier envelope $\hat{p}_h(t)$, we obtain the temporal cross-correlation $R_a(\tau_c) = \langle p_b(t)\hat{p}_h(t-\tau_c)\rangle$; when normalized with the standard deviations, we obtain the normalized correlation coefficient, $\rho_a(\tau_c) \in [-1,1]$. Finally, two modulation metrics are defined: the correlation strength, $\rho_a = \max[\rho(\tau_c)]$, and the phase $\phi_a = \tau_{\mathrm{cm}} f_b(2\pi)$, where τ_{cm} is the temporal shift for which the maximum correlation value occurs. Since the correlation metric involves the BPF-harmonic, correlation maxima occur periodically (see, for instance, Fig. 11 in [38]). This implies that the temporal shift cannot be determined uniquely, but up to an integer multiple of the blade-passage period, so $\phi_a/(2\pi) \pm 1$.

Note that all modulation metrics considered in the current work are correlation-based and energy-normalized (Γ^2_m, ρ_a, and ϕ_a). Hence, the acoustic pressure decay is irrelevant, and the analysis is applicable to a single acoustic pressure time series anywhere in the acoustic near- or far-field regions. All three metrics are computed for each of the 1120 acoustic signals, and the results for two advance ratios, $J = 0$ and 0.41, are shown in Figs. 12 and 13, respectively.

It is apparent that metrics Γ^2_m and ρ_a show similar patterns for $J = 0.41$, thus highlighting the robustness of the two metrics to capture the BPFM strength. Moreover, the strength is considerably weaker for $J = 0$. Later on, in this section, we detail the difference in BPFM strength for changes in the advance ratio. When we here focus on the $J = 0.41$ case with its pronounced BPFM strength, it is seen that the metrics are maximum for $\theta \approx -14°$ (gray dashed line in Figs. 13a and 13b). This will result in a distinguishable intensity modulation of the noise at that polar angle. The strength of BPFM remains constant with outward distance. Even though this is expected for a pure convective acoustic wave field, it was never shown explicitly. It furthermore validates the quality of the acoustic data in the free-field simulated environment; e.g., the modulation is *not* related to nodes or antinodes caused by reflections and constructive/destructive interference of acoustic waves.

The phase relationship between modulating and carrier signals is shown in Fig. 13c and is important for auralization methodologies [19]. An out-of-phase behavior corresponds to a phase of $\phi_a = 0.5(2\pi)$, which would mean that the BPF signal leads (or lags) the occurrence of highest intensity in p_{10f_b} by half-a-period of the BPF. For the sector where the BPFM strength is large (say, $-45° \lesssim \theta \lesssim 0°$), the phase in Fig. 13c equals roughly $\phi_a = 0.25(2\pi) \pm 2\pi$: the BPF signal thus leads the associated, periodic intensity variation in the high-frequency noise by a quarter period of the BPF (or lags by a three-quarter period). This temporal offset, either a lead or lag, is also apparent from the mic. C signal in Fig. 10c.

It is important to realize that Γ^2_m is derived from the magnitude of the auto-bicoherence (and here does not include phase information of the underlying auto-bispectrum). In addition, even though the magnitude of the auto-bicoherence γ^2_{ppp} is normalized for each frequency

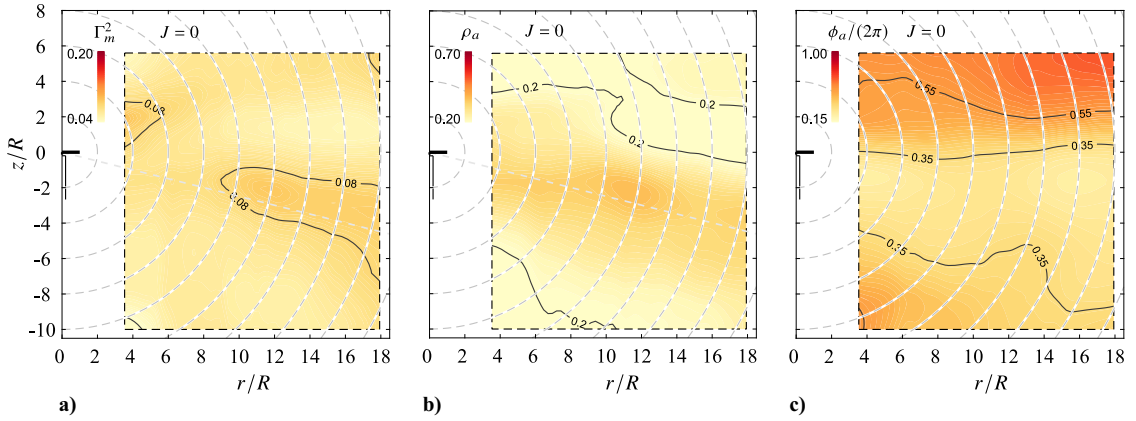

Fig. 12 For the case of $J = 0$, spatial topographies of a) the auto-bicoherence-based metric Γ_m^2, b) the modulation strength ρ_a, and c) the relative phase ϕ_a between modulating and carrier signals.

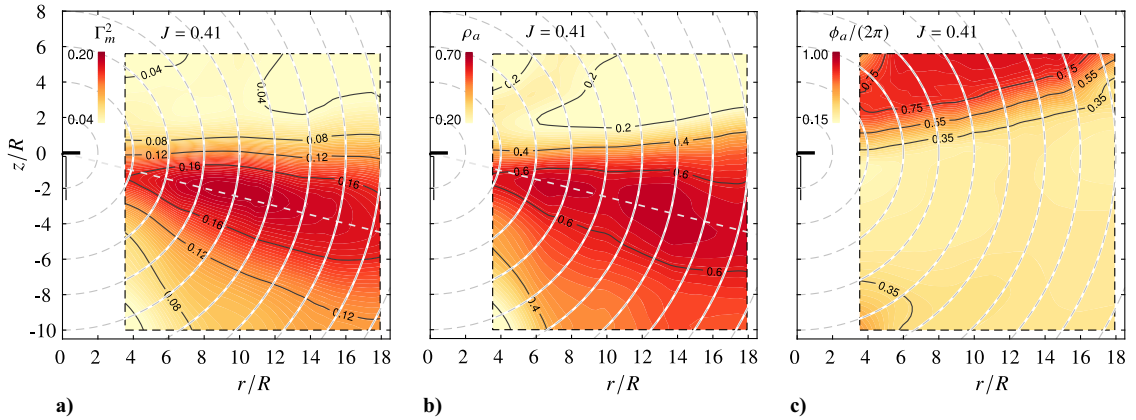

Fig. 13 Similar to Fig. 12, but now for $J = 0.41$.

combination f_1, f_2, the metric involving the entire high-frequency (broadband) range, Γ_m^2, is formed from an arithmetic mean of γ_{ppp}^2. This yields difficulty in interpreting its magnitude. As such, the strength of BPFM is quantified by ρ_a and ϕ_a in the remainder of this work. That is, the phase of the frequency content in the total carrier signal, relative to the modulating signal, was preserved in the two-point correlation analysis through the identification of ϕ_a, while Γ_m^2 is a measure of the phase-coupling on a per-frequency basis.

In order to infer the influence of the advance ratio J on BPFM, similar results were constructed as the ones shown in Figs. 12 and 13, but now for all four advance ratios. Since it was further confirmed that the metrics were invariant with outward radial distance ρ, the directivity patterns of the metrics are presented with polar plots. Figures 14a and 14b show the directivity patterns of ρ_a and ϕ_a, respectively. Individual data points are shown with small markers, as well as a fit line through these data for each J. Observations on the BPFM-directivity patterns can be summarized as follows and will be described in terms of the underlying source mechanisms in Sec. IV.

i) Current directivity patterns confirm earlier observations of BPFM for a hovering rotor ($J = 0$): modulation is predominantly present within the downstream sector, with a maximum strength toward $\theta \approx -20°$. Still, a small degree of BPFM is present above the rotor disk plane.

ii) For the nonzero advance ratios, the BPFM remains weak above the rotor, and the phase reaches a near-constant value of $\phi_a \approx 0.8(2\pi)$.

iii) Below the rotor plane, the BPFM is significantly stronger for the nonzero advance ratios. In the sector of $-45° \lesssim \theta \lesssim -5°$ the BPFM strength slightly increases from $J = 0.24$ to $J = 0.61$ (the highest advance ratio tested), although the overall directivity pattern is very similar. The maximum strength resides around $\theta = -14°$ for all nonzero J, and the associated phase remains constant at a temporal shift of $\phi_a \approx 0.25(2\pi)$.

IV. Source Mechanisms of BPF Modulation

One driving factor involved in the BPFM can be thought of as the periodic variation in the source–receiver distance and convective amplification. However, these effects alone would be most pronounced at sideline angles within the rotor disk plane. Given that the BPFM strength was identified to be maximum in the downstream region, the variations in source–receiver distance and convective amplification cannot be the root cause of BPFM. In an attempt to unravel the mechanisms at play, we first focus on the high-frequency noise content of rotor noise signals. High-frequency noise can primarily come from two source mechanisms: 1) a leading-edge noise mechanism associated with the ingestion of velocity perturbations [58–60], and 2) a trailing-edge mechanism by which noise is generated from turbulent pressure fluctuations convecting past the rotor's trailing edge [61]. In both of these cases, the noise is considered to be high in frequency, given the much lower BPF and the blade's relative velocity.

First, when concentrating on the leading-edge source mechanism that is dominant at $J = 0$, we concentrate on the blade encountering an interference with turbulence from the preceding blade's wake, around the midspan and outboard part of the blade (see the discussion in Sec. II.D and Fig. 9). This leading-edge noise comprises strong harmonics in the midfrequency range (around $f/f_b = 10$), which originate primarily from the blade tip due to the large incoming velocity. This component of leading-edge noise that is dictated mostly by a change in angle of attack radiates rather omnidirectionally due to the compact nature of the thickness noise determined by a BWI source. When considering side and top views in a reference frame fixed to the rotor, the noise directivity patterns of this leading-edge noise are schematically drawn in Figs. 15a and 15b, respectively. When a fixed observer in the acoustic far field experiences a sweep through the directivity pattern due to the rotating blades, the

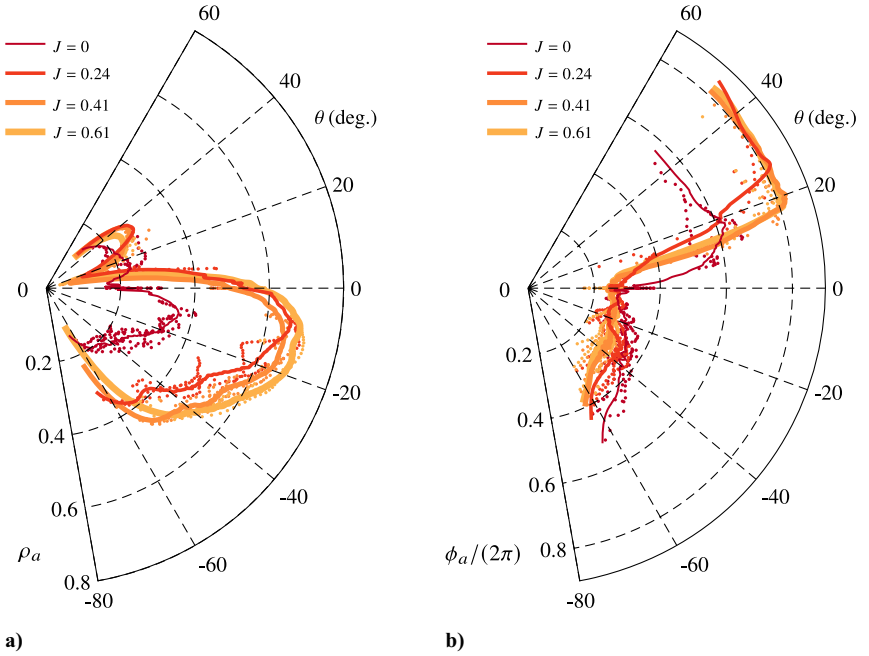

Fig. 14 Directivity patterns of BPFM, for all four advance ratios J, within a) the modulation strength ρ_a, and b) the relative phase ϕ_a between modulating and carrier signals.

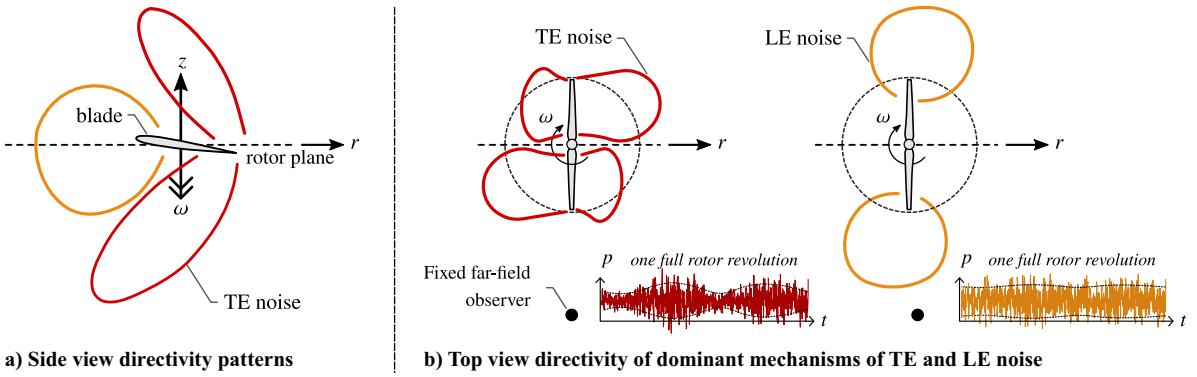

a) Side view directivity patterns **b) Top view directivity of dominant mechanisms of TE and LE noise**

Fig. 15 Schematic illustration of directivity patterns in the context of high-frequency noise, from both trailing-edge (TE) and leading-edge (LE) mechanisms.

BPFM is relatively weak (compared to the trailing-edge component described next).

Secondly, the dominant source of trailing-edge noise is considered. In the case of low-Reynolds-number rotors, this trailing-edge mechanism is governed by the shedding of vortices past the trailing edge (thus scattering sound and being responsible for the high-frequency hump experiences in the far-field acoustic spectra). These vortices themselves result from the vortex shedding from the laminar separation bubble at the suction side of the rotor blade [30]. When considering the side view in a reference frame that is fixed to the rotor (Fig. 15a), this trailing-edge noise directivity tilts forward. Since the vortex shedding is relatively coherent along the span of the blade, the noise-directivity pattern as seen from a top view (Fig. 15b) manifests itself with a main lobe being concentrated along the direction normal to the blade's chord line [61]. As a consequence of the rotor blade spinning, a far-field observer experiences a sweep through this directive noise pattern, thus resulting in a strong BPFM.

When first focusing on the BPFM trends for nonzero advance ratios, the leading-edge noise source mechanism related to BWI is absent (particularly for the two highest advance ratios, recall the discussion of Fig. 9). As such, the modulation is strong since the high-frequency noise content is dominated by the very directive trailing-edge noise. These mechanisms include the trailing-edge diffraction of vortices shed from the laminar separation bubbles on the blades' suction side. Specifically, Grande et al. [29,30] found these bubbles for the cases of $J = 0$, 0.24, and 0.41; the bubbles did increase in size when moving toward the trailing edge when the angle of attack was decreasing [30] (when the advance ratio J was increasing). Note though that the Reynolds number in Grande et al. [29,30] was almost a factor of two lower than the one in our study (e.g., $Re_{c75} \approx 8 \cdot 10^4$ vs $Re_{c75} \approx 1.4 \cdot 10^5$ considered here). Nevertheless, given the Reynolds number variation across the entire blade span, separation bubbles are still to be expected, with a similar trend in that they grow with increasing J. Thus, for the cases with the largest separation bubbles, the wake vortex shedding noise is more pronounced. An inspection of acoustic spectra confirms this: Fig. 16 presents acoustic spectra in the upstream (Fig. 16a), sideline (Fig. 16b), and downstream regions (Fig. 16c) for all four advance ratios. Spectra corresponding to the noise floor of the facility (and wind tunnel noise in the case of $J \neq 0$ is) are also shown. The spectrum of the $J = 0.61$ case clearly has a larger amplitude than the $J = 0.24$ and 0.41 cases in the high-frequency part of the spectrum.

When concentrating on the hover case ($J = 0$), the directive trailing-edge noise source mechanisms are still present. However, the noise content at the high-frequency portion of the spectrum is dominated by the leading-edge mechanism of impinging turbulence coming from the preceding blade's wake. As such, the perception of

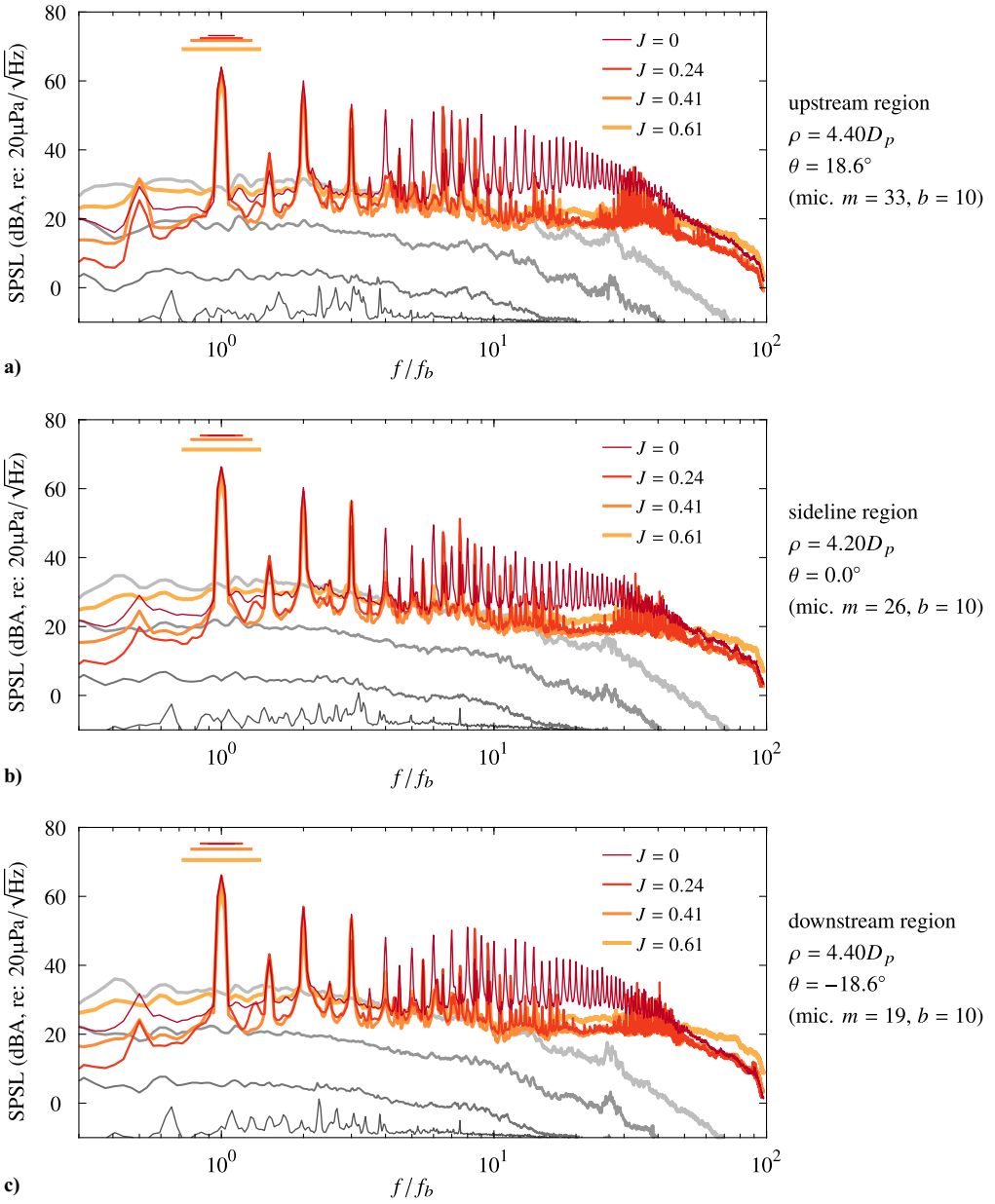

Fig. 16 Acoustic spectra in the a) upstream, b) sideline, and c) downstream regions of the acoustic field for all four J. All spectra are corrected for atmospheric absorption and are A-weighted. SPSL magnitudes of the BPF (horizontal bars) were described in Sec. II.C.

modulation is less than in the advance ratio cases, for which the directive trailing edge dominates the high-frequency portion of the acoustic spectra.

V. Conclusions

A comprehensive study was presented on how the advance ratio (and the associated change in noise source mechanisms) influences the so-called blade passage frequency modulation (BPFM). This phenomenon encompasses a temporal variation in the rotor-noise intensity—with a time scale associated with the BPF—experienced at a fixed position relative to the rotor. Correlation-based metrics were successfully applied to high-fidelity acoustic datasets, spanning both the near- and far-field regions of an isolated rotor.

For the hover scenario, the (modulated) high-frequency noise content originates predominantly from a BWI, a source mechanism affiliated with the leading edge of the rotor blade, and the tip vortex from the preceding blade residing in close proximity to the successive blade. It was conjectured that the relatively omnidirectional noise directivity of this leading-edge mechanism, dominated by the rotor-tip blade region, results in a relatively weak modulation of the high-frequency noise for a stationary far-field observer.

For nonzero advance ratios, noise scattering at the trailing-edge caused by the vortex shedding of laminar separation bubbles yields a relatively directive noise component at high frequencies. It was hypothesized that the appearance of a strong BPFM is in this case a direct consequence of an acoustic observer—at a fixed position relative to the rotor—experiencing sweeps through the directivity pattern of this trailing-edge noise (fixed to the spinning rotor blade). Since this trailing-edge noise component intensifies with increasing advance ratio, the degree of modulation also becomes largest for the highest advance ratio tested ($J = 0.61$). For the particular benchmark rotor under investigation, this advance ratio corresponds to a maximum in the propulsive efficiency.

Future work could strengthen our hypothesis by incorporating reduced-order models of the broadband noise sources into predictive tools for tonal noise content. One approach to achieve this is by implementing an acoustic radiation model for the tonal noise contribution, along with empirical directivity patterns of the leading- and trailing-edge noise sources. The former follows from a time-domain Ffowcs-Williams and Hawking's acoustic analogy (e.g., based on a

compact dipole/monopole formulation used in the literature [62,63]). Future research on human perception and annoyance should explore the relationship between engineering BPFM metrics and psychoacoustic metrics. Establishing this connection would allow BPFM metrics to facilitate the assessment of the noise impact of AAM vehicles. This could be accomplished, for instance, by applying the BPFM metrics to data from high-fidelity numerical computations of rotor noise [64–66] or other noise prediction frameworks [20,67–70].

Appendix: Bispectral Analysis for Computing a Modulation Metric

Through a bispectral analysis, the dominant quadratic interfrequency coupling can be found out of all possible frequency combinations present within a signal (here taken as p and its Fourier transform, $P(f) = \mathcal{F}[p(t)]$). This analysis effectively correlates two frequency components, f_1 and f_2, to their sum ($f_3 = f_1 + f_2$) or difference and can be expressed as an auto-bicoherence, $\gamma^2_{\mathrm{ppp}}(f_1, f_2)$, according to

$$\gamma^2_{\mathrm{ppp}} = \frac{|\phi_{\mathrm{ppp}}(f_1, f_2)|^2}{\phi_{\mathrm{pp}}(f_1)\phi_{\mathrm{pp}}(f_2)\phi_{\mathrm{pp}}(f_1 + f_2)} \in [0, 1] \tag{A1}$$

Here, the numerator is the auto-bispectrum, taken as $\phi_{\mathrm{ppp}}(f_1, f_2) = 2\langle P(f_1 + f_2)P^*(f_1)P^*(f_2)\rangle$. Note that $\gamma^2_{\mathrm{ppp}}(f_1, f_2)$ indicates the degree of normalized correlation between the energy at f_1 and f_2, and the energy at $f_1 + f_2$ (here we only consider sum-interactions). An example auto-bicoherence spectrum is shown in Fig. A1a for microphone C and for $J = 0$. Typically, a ridge is shown to have relatively strong bicoherence along $f_2 = f_b$. Since this means that the BPF is phase-coupled to a broad range of frequencies with the same signal (thus to frequencies $f_1 > f_b$), this ridge is representative of the degree of BPFM.

To infer what content in a time series, or autospectrum (plotted in Fig. A1b for the corresponding auto-bicoherence in Fig. A1a), is *involved* in quadratic sum interactions, the 2D auto-bicoherence $\gamma^2_{\mathrm{ppp}}(f_1, f_2)$ can be condensed to a one-dimensional summed bicoherence [71,72]. This is done by averaging along lines of constant $f = f_1 + f_2$:

$$\Gamma^2_{\mathrm{ppp}}(f) = \frac{1}{N_q(f)} \sum_{f=f_1+f_2} \gamma^2_{\mathrm{ppp}}(f_1, f_2) \tag{A2}$$

Here, $N_q(f)$ is the number of frequency doublets f_1, f_2. This summed bicoherence spectrum is shown in Fig. A1c, and its frequency axis is aligned with the auto spectrum in Fig. A1b. It is evident that Γ^2_{ppp} shows the degree of nonlinear interactions that are buried in certain frequency components (but for their f_1 and f_2 origin it is necessary to reside back to Fig. A1a). On a final note, the summed bicoherence spectrum is also plotted for a generated reference signal comprising random noise (uncorrelated in a linear and nonlinear

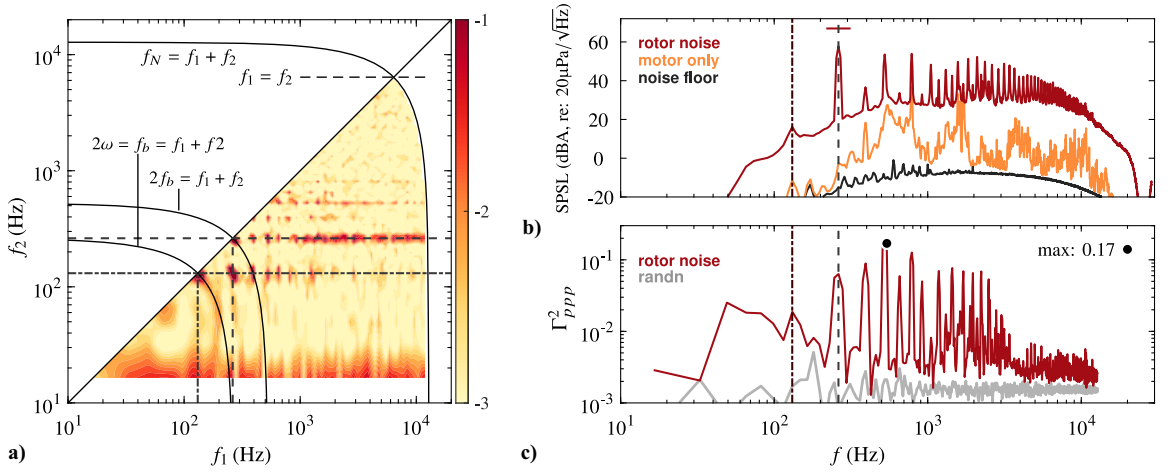

Fig. A1 a) Contour of the auto-bicoherence $\log_{10}[\gamma^2_{\mathrm{ppp}}]$ generated from the time series of microphone C, for $J = 0$. b) Corresponding acoustic spectra at microphone position C, with alongside in (c) the summed auto-bicoherence $\Gamma^2_{\mathrm{ppp}}(f = f_1 + f_2)$ for the rotor noise, and for a reference signal comprising random noise.

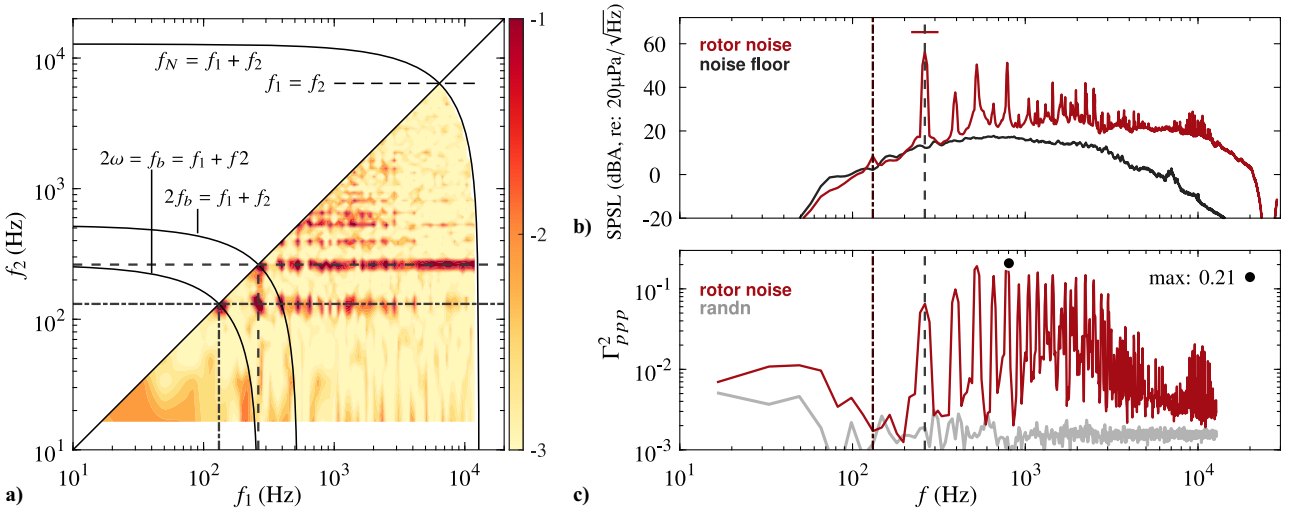

Fig. A2 Similar to Fig. 18, but now for $J = 0.41$.

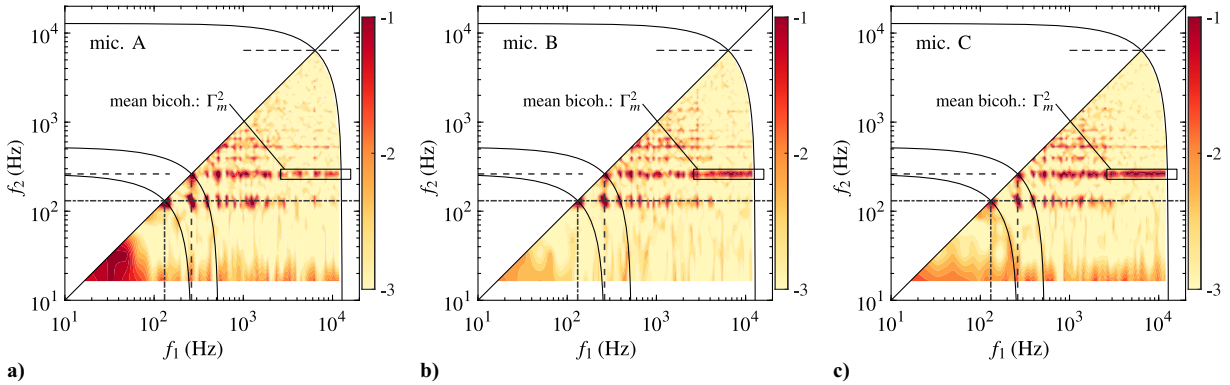

Fig. A3 a–c) Contours of auto-bicoherence $\log_{10}[\gamma^2_{ppp}]$ at microphone positions A, B, and C, comprising triadic sum interactions, $f = f_1 + f_2$. A rectangular box signifies the portion of the auto-bicoherence used in forming Γ^2_m.

way), highlighting that the bicoherence in the rotor noise signal is significant; it was furthermore ensured that all results of our bispectral analysis are converged [51].

For further inspection and in the context that BPFM modulation appears stronger for $J = 0.41$, in comparison to $J = 0$, plots similar to the ones presented in Fig. A1 are shown in Fig. A2, but now for $J = 0.41$. It is apparent that the ridge of bicoherence along $f_2 = f_b$ is higher in magnitude, particularly for the higher frequencies, $f_1 > 10f_b$.

Given that the auto-bicoherence helps in forming a holistic view on the degree of phase coupling, we can define a single metric when considering the BPF tone as one of the primary frequencies forming all possible quadratic frequency doublets. For this, we take the mean value of the auto-bicoherence along $f_2 = f_b$ and for all quadratic frequency doublets residing at $f_1 > 10f_b$, according to

$$\Gamma^2_m = \frac{1}{N_a} \sum_{f_1 > 10f_b} \gamma^2_{\mathrm{ppp}}(f_1, f_2 = f_b) \tag{A3}$$

Γ^2_m is a measure for the degree of phase coupling between the noise at $f > 10f_b$ and the BPF tone at $f = f_b$ (N_a is the number of discrete points over which the auto-bicoherence is summed). From a preliminary assessment of the auto-bicoherence and parameter Γ^2_m at positions A, B, and C for $J = 0.41$ (Fig. A3), it is evident that Γ^2_m is varying in the field (e.g., Γ^2_m is minimum at position A and maximum at position C).

Acknowledgments

The authors wish to gratefully acknowledge Edoardo Grande for assisting in the experiments and for stimulating discussions about the content of this paper. The authors would also like to give special thanks to Tomas Sinnige for setting up the power supply and the RPM-control capability of the rotor.

References

[1] Tegler, J., "Noise Alert!" Aerospace America, AIAA, Vol. 58, No. 4, 2020, https://aerospaceamerica.aiaa.org/features/noise-alert/.

[2] Ol, M., Zeune, C., and Logan, M., "Analytical/Experimental Comparison for Small Electric Unmanned Air Vehicle Propellers," AIAA Paper 2008-7345, 2008. https://doi.org/10.2514/6.2008-7345

[3] Brandt, J. B., and Selig, M. S., "Propeller Performance Data at Low Reynolds Numbers," AIAA Paper 2011-1255, 2011. https://doi.org/10.2514/6.2011-1255

[4] Sinibaldi, G., and Marino, L., "Experimental Analysis on the Noise of Propellers for Small UAV," *Applied Acoustics*, Vol. 74, No. 1, 2013, pp. 79–88. https://doi.org/10.1016/j.apacoust.2012.06.011

[5] Zawodny, N. S., and Boyd, D. D., Jr., "Investigation of Rotor-Airframe Interaction Noise Associated with Small-Scale Rotary-Wing Unmanned Aircraft Systems," VFS 73rd Annual Forum, NF1676L-25342, Vertical Flight Library & Store, 2017.

[6] Tinney, C. E., and Sirohi, J., "Multirotor Drone Noise at Static Thrust," *AIAA Journal*, Vol. 56, No. 7, 2018, pp. 2816–2826. https://doi.org/10.2514/1.J056827

[7] Tinney, C. E., and Valdez, J., "Acoustic Scaling for Small Rotors in Hover," VFS 75th Annual Forum, Vertical Flight Library & Store, 2019. https://doi.org/10.4050/F-0075-2019-14457

[8] Alexander, W. N., Whelchel, J., Intaratep, N., and Trani, A., "Predicting Community Noise of sUAS," AIAA Paper 2019-2686, 2019. https://doi.org/10.2514/6.2019-2686

[9] Jordan, W., Narsipur, S., and Deters, R. W., "Aerodynamic and Aeroacoustic Performance of Small UAV Propellers in Static Conditions," AIAA Paper 2020-2595, 2020. https://doi.org/10.2514/6.2020-2595

[10] Yang, Y., Liu, Y., Li, Y., and Arcondoulis, E., "Aerodynamic and Aeroacoustic Performance of an Isolated Multicopter Rotor During Forward Flight," *AIAA Journal*, Vol. 58, No. 3, 2020, pp. 1171–1181. https://doi.org/10.2514/1.J058459

[11] Tinney, C. E., and Valdez, J., "Thrust and Acoustic Performance of Small-Scale, Coaxial, Corotating Rotors in Hover," *AIAA Journal*, Vol. 58, No. 4, 2020, pp. 1657–1667. https://doi.org/10.2514/1.J058489

[12] Valdez, J. A., and Tinney, C. E., "Wake of a Coaxial Corotating Rotor in Hover," *AIAA Journal*, Vol. 60, No. 8, 2022, pp. 4829–4839. https://doi.org/10.2514/1.J061651

[13] Christian, A., and Cabell, R., "Initial Investigation into the Psychoacoustic Properties of Small Unmanned Aerial System Noise," AIAA Paper 2017-4051, 2017. https://doi.org/10.2514/6.2017-4051

[14] Rizzi, S. A., Palumbo, D. L., Rathsam, J., Christian, A. W., and Rafaelof, M., "Annoyance to Noise Produced by a Distributed Electric Propulsion High-Lift System," AIAA Paper 2017-4050, 2017. https://doi.org/10.2514/6.2017-4050

[15] Zawodny, N. S., and Pettingill, N. A., "Acoustic Wind Tunnel Measurements of a Quadcopter in Hover and Forward Flight Conditions," *INTER-NOISE and NOISE-CON Congress and Conference Proceedings*, InterNoise 18, Chicago, IL, Inst. of Noise Control Engineering, 2018, pp. 1–993, https://www.ingentaconnect.com/contentone/ince/incecp/2018/00000258/00000007/art00049.

[16] Krishnamurthy, S., Christian, A., and Rizzi, S. A., "Psychoacoustic Test to Determine Sound Quality Metric Indicators of Rotorcraft Noise Annoyance," *International Congress and Exposition on Noise Control Engineering*, Rept. NF1676L-29456, Inst. of Noise Control Engineering, Aug. 2018, https://www.ingentaconnect.com/contentone/ince/incecp/2018/00000258/00000007/art00032.

[17] Christian, A., Caston, J., and Greenwood, E., "Regarding the Perceptual Significance and Characterization of Broadband Components of Helicopter Source Noise," *VFS 75th Annual Forum*, Vertical Flight Library & Store, 2019. https://doi.org/10.4050/F-0075-2019-14449

[18] Gan, Z. F. T., Brentner, K. S., and Greenwood, E., "Time Variation of Helicopter Broadband Noise," AIAA Paper 2022-2914, 2022. https://doi.org/10.2514/6.2022-2914

[19] Krishnamurthy, S., and Rizzi, S. A., "Auralization of Amplitude Modulated Helicopter Flyover Noise," AIAA Paper 2019-2087, 2019. https://doi.org/10.2514/6.2019-2087

[20] Han, D., Gwak, D. Y., and Lee, S., "Noise Prediction of Multi-Rotor UAV by RPM Fluctuation Correction Method," *Journal of Mechanical Science and Technology*, Vol. 34, No. 4, 2020, pp. 1429–1443. https://doi.org/10.1007/s12206-020-0305-2

[21] Li, S., and Lee, S., "A Machine Learning-Based Fast Prediction of Rotorcraft Broadband Noise," AIAA Paper 2020-2588, 2020. https://doi.org/10.2514/6.2020-2588

[22] Torija, A. J., and Clark, C., "A Psychoacoustic Approach to Building Knowledge About Human Response to Noise of Unmanned Aerial Vehicles," *International Journal of Environmental Research and Public Health*, Vol. 18, No. 682, 2021, pp. 1–16. https://doi.org/10.3390/ijerph18020682

[23] Torija, A. J., Chaitanya, P., and Li, Z., "Psychoacoustic Analysis of Contra-Rotating Propeller Noise for Unmanned Aerial Vehicles," *Journal of the Acoustical Society of America*, Vol. 149, No. 2, 2021, pp. 835–846. https://doi.org/10.1121/10.0003432

[24] Torija, A. J., Li, Z., and Chaitanya, P., "Psychoacoustic Modelling of Rotor Noise," *Journal of the Acoustical Society of America*, Vol. 151, No. 3, 2022, pp. 1804–1815. https://doi.org/10.1121/10.0009801

[25] Marte, J. E., and Kurtz, D. W., "A Review of Aerodynamic Noise from Propellers, Rotors, and Lift Fans," NASA TR-32-1462, 1970, https://ntrs.nasa.gov/citations/19700005920.

[26] Amiet, R. K., "Noise Produced by Turbulent Flow into a Propeller or Helicopter Rotor," *AIAA Journal*, Vol. 15, No. 3, 1977, pp. 307–308. https://doi.org/10.2514/3.63237

[27] Glegg, S., and Devenport, W., "Open Rotor Noise," Aeroacoustics of Low Mach Number Flows, Academic Press, Elsevier, Amsterdam, 2017, pp. 399–436, Chap. 16.

[28] Candeloro, P., Pagliaroli, T., Ragni, D., and Di Francesco, S., "Small-Scale Rotor Aeracoustics for Drone Propulsion: A Review of Noise Sources and Control Strategies," *Fluids*, Vol. 7, No. 8, 2022, p. 279. https://doi.org/10.3390/fluids7080279

[29] Grande, E., Romani, G., Ragni, D., Avallone, F., and Casalino, D., "Aeroacoustic Investigation of a Propeller Operating at Low Reynolds Numbers," *AIAA Journal*, Vol. 60, No. 2, 2022, pp. 860–871. https://doi.org/10.2514/1.J060611

[30] Grande, E., Ragni, D., Avallone, F., and Casalino, D., "Laminar Separation Bubble Noise on a Propeller Operating at Low Reynolds Numbers," *AIAA Journal*, Vol. 60, No. 9, 2022, pp. 5324–5335. https://doi.org/10.2514/6.2022-2940

[31] Stephenson, J. H., Tinney, C. E., Greenwood, E., and Watts, M. E., "Time Frequency Analysis of Sound from a Maneuvering Rotorcraft," *Journal of Sound and Vibration*, Vol. 333, No. 21, 2014, pp. 5324–5339. https://doi.org/10.1016/j.jsv.2014.05.018

[32] Rizzi, S. A., Zawodny, N. S., and Pettingill, N. A., "On the Use of Acoustic Wind Tunnel Data for the Simulation of sUAS Flyover Noise," AIAA Paper 2019-2630, 2019. https://doi.org/10.2514/6.2019-2630

[33] Hubbard, H. H., "Aeroacoustics of Flight Vehicles: Theory and Practice Volume 1: Noise Sources," NASA TR-90-3052, 1990, https://ntrs.nasa.gov/citations/19920001380.

[34] Baars, W. J., and Tinney, C. E., "Shock-Structures in the Acoustic Field of a Mach 3 Jet with Crackle," *Journal of Sound and Vibration*, Vol. 333, No. 12, 2014, pp. 2539–2553. https://doi.org/10.1016/j.jsv.2014.01.008

[35] Jurdic, V., Joseph, P., and Antoni, J., "Investigation of Rotor Wake Turbulence Through Cyclostationary Spectral Analysis," *AIAA Journal*, Vol. 47, No. 9, 2009, pp. 2022–2030. https://doi.org/10.2514/1.36728

[36] Meloni, S., de Paola, E., Grande, E., Ragni, D., Stoica, L. G., Di Marco, A., and Camussi, R., "A Wavelet-Based Separation Method for Tonal and Broadband Components of Low Reynolds-Number Propeller Noise," *Measurement Science and Technology*, Vol. 34, No. 4, 2023, Paper 044007. https://doi.org/10.1088/1361-6501/acb071

[37] Tinney, C. E., Valdez, J. A., and Zhao, Y., "A Moving Source Model for Rotor Broadband Noise," AIAA Paper 2023-3222, 2023. https://doi.org/10.2514/6.2023-3222

[38] Baars, W. J., Bullard, L., and Mohamed, A., "Quantifying Modulation in the Acoustic Field of a Small-Scale Rotor Using Bispectral Analysis," AIAA Paper 2021-0713, 2021. https://doi.org/10.2514/6.2021-0713

[39] Rizzi, S. A., Huff, D. L., Boyd, D. D., Bent, P., Henderson, B. S., Pascioni, K. A., Sargent, D. C., Josephson, D. L., Marsan, M., He, H. B., et al., "Urban Air Mobility Noise: Current Practice, Gaps, and Recommendations," NASA TR-32-1462, 2020, https://ntrs.nasa.gov/citations/20205007433.

[40] Greenwood, E., Brentner, K. S., Rau, R. F., and Gan, Z. F. T., "Challenges and Opportunities for Low Noise Electric Aircraft," *International Journal of Aeroacoustics*, Vol. 21, Nos. 5–7, 2022, pp. 315–381. https://doi.org/10.1177/1475472X2211073

[41] Merino-Martínez, R., Carpio, A. R., Pereira, L. T. L., van Herk, S., Avallone, F., Ragni, D., and Kotsonis, M., "Aeroacoustic Design and Characterization of the 3D-Printed, Open-Jet, Anechoic Wind Tunnel of Delft University of Technology," *Applied Acoustics*, Vol. 170, Dec. 2020, Paper 107504. https://doi.org/10.1016/j.apacoust.2020.107504

[42] Stephenson, J. H., Weitsman, D., and Zawodny, N. S., "Effects of Flow Recirculation on Unmanned Aircraft System (UAS) Acoustic Measurements in Closed Anechoic Chambers (L)," *Journal of the Acoustical Society of America*, Vol. 145, No. 3, 2019, pp. 1153–1155. https://doi.org/10.1121/1.5092213

[43] Weitsman, D., Stephenson, J. H., and Zawodny, N. S., "Effects of Inflow Recirculation on Acoustic and Dynamic Measurements of Rotary-Wing Systems Operating in Closed Anechoic Chambers," *Journal of the Acoustical Society of America*, Vol. 148, No. 3, 2020, pp. 1325–1336. https://doi.org/10.1121/10.0001901

[44] Casalino, D., Romani, G., Pii, L. M., and Colombo, R., "Flow Confinement Effects on sUAS Rotor Noise," *Aerospace Science and Technology*, Vol. 143, Dec. 2023, Paper 108756. https://doi.org/10.1016/j.ast.2021.106707

[45] Casalino, D., Grande, E., Romani, G., Ragni, D., and Avallone, F., "Definition of a Benchmark for Low Reynolds Number Propeller Aeroacoustics," *Aerospace Science and Technology*, Vol. 113, June 2021, Paper 106707. https://doi.org/10.1016/j.ast.2021.106707

[46] Deters, R. W., Ananda, G. K., and Selig, M. S., "Reynolds Number Effects on the Performance of Small-Scale Propellers," AIAA Paper 2014-2151, 2014. https://doi.org/10.2514/6.2014-2151

[47] Gojon, R., Jardin, T., and Parisot-Dupuis, H., "Experimental Investigation of Low Reynolds Number Rotor Noise," *Journal of the Acoustical Society of America*, Vol. 149, No. 6, 2021, pp. 3813–3829. https://doi.org/10.1121/10.0005068

[48] Casalino, D., Romani, G., Zhang, R., and Chen, H., "Lattice-Boltzmann Calculations of Rotor Aeroacoustics in Transitional Boundary Layer Regime," *Aerospace Science and Technology*, Vol. 130, Nov. 2022, Paper 107953. https://doi.org/10.2514/6.2022-2862

[49] Viswanathan, K., "Instrumentation Considerations for Accurate Jet Noise Measurements," *AIAA Journal*, Vol. 44, No. 6, 2006, pp. 1137–1149. https://doi.org/10.2514/1.13518

[50] Fiévet, R., Tinney, C. E., Baars, W. J., and Hamilton, M. F., "Coalescence in the Sound Field of a Laboratory Scale Supersonic Jet," *AIAA Journal*, Vol. 54, No. 1, 2016, pp. 254–265. https://doi.org/10.2514/1.J054252

[51] Poloskei, P. Z., Papp, G., Por, G., Horvath, L., and Pokol, G. I., "Bicoherence Analysis of Nonstationary and Nonlinear Processes," arXiv:1811.02973 [eess.SP], 2018, https://arxiv.org/abs/1811.02973.

[52] Fletcher, H., and Munson, W. A., "Loudness, Its Definition, Measurement and Calculation," *Journal of the Acoustical Society of America*, Vol. 5, Oct. 1933, pp. 82–108. https://doi.org/10.1121/1.1915637

[53] Amiet, R. K., "Refraction of Sound by a Shear Layer," *Journal of Sound and Vibration*, Vol. 58, No. 4, 1978, pp. 467–482. https://doi.org/10.1016/0022-460X(78)90353-X

[54] Huff, D. L., and Henderson, B. S., "Electric Motor Noise for Small Quadcopters: Part 1–Acoustic Measurements," AIAA Paper 2018-2952, 2018. https://doi.org/10.2514/6.2018-2952

[55] Henderson, B. S., Huff, D., Cluts, J., and Ruggeri, C., "Electric Motor Noise for Small Quadcopters: Part II–Source Characteristics and Predictions," AIAA Paper 2018-2953, 2018. https://doi.org/10.2514/6.2018-2953

[56] Brentner, K. S., and Farassat, F., "Modeling Aerodynamically Generated Sound of Helicopter Rotors," *Progress in Aerospace Sciences*, Vol. 39, Nos. 2–3, 2003, pp. 83–120. https://doi.org/10.1016/S0376-0421(02)00068-4

[57] Thurman, C. S., and Baeder, J. D., "Blade-Wake Interaction Noise for Small Hovering Rotors, Part I: Characterization Study," *AIAA Journal*, Vol. 61, No. 6, 2023, pp. 2552–2569. https://doi.org/10.2514/1.J062565

[58] Sevik, M., "Sound Radiation from a Subsonic Rotor Subjected to Turbulence," *Fluid Mechanics, Acoustics, and Design of Turbomachinery, Pt. 2*, Vol. 34, No. 2, 1974, pp. 493–512, https://ntrs.nasa.gov/citations/19750003123.

[59] Hanson, D. B., "Spectrum of Rotor Noise Caused by Atmospheric Turbulence," *Journal of the Acoustical Society of America*, Vol. 56, No. 1, 1974, pp. 110–126. https://doi.org/10.1121/1.1903241

[60] Amiet, R. K., "Acoustic Radiation from an Airfoil in a Turbulent Stream," *Journal of Sound and Vibration*, Vol. 41, No. 4, 1975, pp. 407–420.
https://doi.org/10.1016/S0022-460X(75)80105-2

[61] Amiet, R. K., "Noise Due to Turbulent Flow Past a Trailing Edge," *Journal of Sound and Vibration*, Vol. 47, No. 3, 1976, pp. 387–393.
https://doi.org/10.1016/0022-460X(76)90948-2

[62] Casalino, D., Barbarino, M., and Visingardi, A., "Simulation of Helicopter Community Noise in a Realistic Urban Environment," AIAA Paper 2010-4004, 2010.
https://doi.org/10.2514/6.2010-4004

[63] Fuerkaiti, Y., Grande, E., Casalino, D., Avallone, F., and Ragni, D., "Efficient Low-Fidelity Aeroacoustic Permanence Calculation of Propellers," *Aerospace Science and Technology*, Vol. 123, April 2022, Paper 107438.
https://doi.org/10.1016/j.ast.2022.107438

[64] Henricks, Q., Wang, Z., and Zhuang, M., "Small-Scale Rotor Design Variables and Their Effects on Aerodynamic and Aeroacoustic Performance of a Hovering Rotor," *Journal of Fluids Engineering*, Vol. 142, No. 8, 2020, Paper 081209.
https://doi.org/10.1115/1.4046872

[65] Lee, H., and Lee, D., "Rotor Interactional Effects on Aerodynamic and Noise Characteristics of a Small Multirotor Unmanned Aerial Vehicle," *Physics of Fluids*, Vol. 32, No. 4, 2020, Paper 047107.
https://doi.org/10.1063/5.0003992

[66] Casalino, D., van der Velden, W. C. P., Romani, G., and Gonzales-Martino, I., "Aeroacoustic Analysis of Urban Air Operations Using the LB/VLES Method," AIAA Paper 2019-2662, 2019.
https://doi.org/10.2514/6.2019-2662

[67] Bian, H., Fattah, R., Sun, Y., and Zhang, X., "Noise Prediction of Drones in Urban Environments," AIAA Paper 2019-2685, 2019.
https://doi.org/10.2514/6.2019-2685

[68] Roger, M., and Moreau, S., "Tonal-Noise Assessment of Quadrotor-Type UAV Using Source-Mode Expansions," *Acoustics*, Vol. 2, No. 3, 2020, pp. 674–690.
https://doi.org/10.3390/acoustics2030036

[69] Sagaga, J. D. W., and Lee, S., "CFD Hover Predictions for the Side-by-Side Urban Air Taxi Concept Rotor," AIAA Paper 2020-2795, 2020.
https://doi.org/10.2514/6.2020-2795

[70] Thurman, C. S., Boyd, D. D., Jr., and Simmons, B. M., "Comparison of Prediction Modeling Methodologies for Aeroacoustic Characterization of Hovering sUAS Rotors," AIAA Paper 2023-0027, 2023.

[71] Procházka, A., Uhlíř, J., Rayner, P. W. J., and Kingsbury, N. G., "Signal Analysis and Prediction," *Higher-Order Statistics in Signal Processing Chapter*, Springer Link, Birkhauser, Longman Cheshire, Melbourne, Australia, 1998, pp. 57–77.

[72] Baars, W. J., and Tinney, C. E., "Proper Orthogonal Decomposition-Based Spectral Higher-Order Stochastic Estimation," *Physics of Fluids*, Vol. 26, No. 5, 2014, Paper 055112.
https://doi.org/10.1063/1.4879255

M. M. Choudhari
Associate Editor